CrossMark

The Habitable Zone Planet Finder Reveals a High Mass and Low Obliquity for the Young Neptune K2-25b

Gudmundur Stefansson[1,2,3,18,19] , Suvrath Mahadevan[1,2] , Marissa Maney[1] , Joe P. Ninan[1,2] , Paul Robertson[4] ,
Jayadev Rajagopal[5], Flynn Haase[5], Lori Allen[5] , Eric B. Ford[1,2,6] , Joshua Winn[3] , Angie Wolfgang[1,2] ,
Rebekah I. Dawson[1,2,20] , John Wisniewski[7], Chad F. Bender[8], Caleb Cañas[1,2,18] , William Cochran[9] ,
Scott A. Diddams[10,11], Connor Fredrick[10,11], Samuel Halverson[12], Fred Hearty[1,2], Leslie Hebb[13] , Shubham Kanodia[1,2] ,
Eric Levi[1], Andrew J. Metcalf[10,11,14] , Andrew Monson[1,2], Lawrence Ramsey[1,2], Arpita Roy[15,21] , Christian Schwab[16] ,
Ryan Terrien[17] , and Jason T. Wright[1,2]

[1] Department of Astronomy & Astrophysics, The Pennsylvania State University, 525 Davey Lab, University Park, PA 16802, USA; gstefansson@astro.princeton.edu
[2] Center for Exoplanets & Habitable Worlds, University Park, PA 16802, USA
[3] Department of Astrophysical Sciences, Princeton University, 4 Ivy Lane, Princeton, NJ 08540, USA
[4] Department of Physics and Astronomy, University of California–Irvine, Irvine, CA 92697, USA
[5] NSF's OIR Lab, 950 North Cherry Avenue, Tucson, AZ 85719, USA
[6] Institute for Computational & Data Sciences, The Pennsylvania State University, 203 Computer Building, University Park, PA 16802, USA
[7] Homer L. Dodge Department of Physics and Astronomy, University of Oklahoma, 440 West Brooks Street, Norman, OK 73019, USA
[8] Steward Observatory, University of Arizona, Tucson, AZ 85721, USA
[9] McDonald Observatory and Center for Planetary Systems Habitability, The University of Texas at Austin, Austin, TX 78712, USA
[10] Time and Frequency Division, National Institute of Standards and Technology, 325 Broadway, Boulder, CO 80305, USA
[11] Department of Physics, University of Colorado, 2000 Colorado Avenue, Boulder, CO 80309, USA
[12] Jet Propulsion Laboratory, California Institute of Technology, 4800 Oak Grove Drive, Pasadena, CA 91109, USA
[13] Department of Physics, Hobart and William Smith Colleges, 300 Pulteney Street, Geneva, NY 14456, USA
[14] Space Vehicles Directorate, Air Force Research Laboratory, 3550 Aberdeen Avenue SE, Kirtland AFB, NM 87117, USA
[15] California Institute of Technology, 1200 East California Boulevard, Pasadena, CA 91125, USA
[16] Department of Physics and Astronomy, Macquarie University, Balaclava Road, North Ryde, NSW 2109, Australia
[17] Department of Physics and Astronomy, Carleton College, Northfield, MN 55057, USA

Abstract

Using radial velocity data from the Habitable Zone Planet Finder, we have measured the mass of the Neptune-sized planet K2-25b, as well as the obliquity of its M4.5 dwarf host star in the 600–800 Myr Hyades cluster. This is one of the youngest planetary systems for which both of these quantities have been measured and one of the very few M dwarfs with a measured obliquity. Based on a joint analysis of the radial velocity data, time-series photometry from the K2 mission, and new transit light curves obtained with diffuser-assisted photometry, the planet's radius and mass are $3.44 \pm 0.12\ R_\oplus$ and $24.5^{+5.7}_{-5.2}\ M_\oplus$. These properties are compatible with a rocky core enshrouded by a thin hydrogen–helium atmosphere (5% by mass). We measure an orbital eccentricity of $e = 0.43 \pm 0.05$. The sky-projected stellar obliquity is $\lambda = 3° \pm 16°$, compatible with spin–orbit alignment, in contrast to other "hot Neptunes" that have been studied around older stars.

1. Introduction

The observed orbital properties of planetary systems are influenced by both the formation process and subsequent dynamical interactions that can take place after planets are formed. Dynamical interactions over billions of years can modify or even rearrange planetary orbits, making it difficult to learn about the initial conditions. Young systems have had less time to evolve, and their orbital properties may provide a clearer view of the early stages of planet formation. As such, young systems are valuable benchmarks for testing models of planet formation and evolution.

The K2 mission (Howell et al. 2014) enabled the detection of many planets in young associations and clusters, including a number of planets discovered by the Zodiacal Exoplanets In Time (ZEIT) project (e.g., Mann et al. 2016a, 2016b, 2017) and the four newborn transiting planets around V1298 Tau (David et al. 2019). The ongoing Transiting Exoplanet Survey Satellite mission (Ricker et al. 2014) is also observing young stars and has led to the discovery of the 45 Myr old Neptune-sized planet DS Tuc Ab (Benatti et al. 2019; Newton et al. 2019) and the 22 Myr old Neptune orbiting the pre-main-sequence star AU Microscopii (AU Mic; Plavchan et al. 2020). Follow-up spectroscopic observations of both DS Tuc Ab (Montet et al. 2020; Zhou et al. 2020) and AU Mic b (Hirano et al. 2010; Addison et al. 2020; Palle et al. 2020) have revealed that both stars have a low obliquity—the angle between its rotation axis and the planet's orbital axis. This is interesting because close-orbiting Neptunes around older stars seem to have a broad

---

range of obliquities (e.g., Winn et al. 2010b; Bourrier et al. 2018b), although the number of measurements is still quite limited.

Both the stellar obliquity and orbital eccentricity are clues about the formation and subsequent dynamical history of planetary systems. For example, based on direct imaging data, Bowler et al. (2020) reported a difference in the eccentricity distributions of planets and brown dwarfs, evidence that these objects form in different ways. Planets are expected to form on circular and coplanar orbits within protoplanetary disks, although they can develop nonzero eccentricities via planet/ planet interactions (Rasio & Ford 1996), secular von Zeipel–Lidov–Kozai cycles (Naoz 2016; Ito & Ohtsuka 2019), planet–disk interactions (Goldreich & Sari 2003), or other dynamical processes. The same dynamical processes can also alter the orbital inclinations of planetary orbits, changing the obliquity of the star (Winn & Fabrycky 2015). In particular, von Zeipel–Kozai–Lidov cycles combined with tidal friction (Fabrycky & Tremaine 2007) can leave a planet stranded on a polar orbit (e.g., GJ 436b; Bourrier et al. 2018b) or even a retrograde orbit (e.g., HAT-P-7b; Winn et al. 2009). Obliquities can be measured by exploiting the Rossiter–McLaughlin (RM) effect, the alteration of the star's absorption line profiles during a planetary transit, which is often manifested as a radial velocity (RV) anomaly (McLaughlin 1924; Rossiter 1924).

Although hundreds of obliquities have been measured with the RM effect, the current list includes only three M dwarfs: GJ 436 (Bourrier et al. 2018a), TRAPPIST-1 (Hirano et al. 2020a), and AU Mic (Addison et al. 2020; Hirano et al. 2020b; Palle et al. 2020). The obliquity of GJ 436b was found to be $\lambda = 72^{+33}_{-24}$°, suggesting a strong misalignment, and AU Mic was found to be well aligned with the equator of its host star. For TRAPPIST-1, the current data are compatible with a low obliquity but with large uncertainties. The RM measurements of M dwarfs have been limited, as they tend to be optically faint, hindering the detection of the RM effect. If we could expand the sample of M dwarfs with measured obliquities, we might be able to gain clues about the dynamical histories of late-type stars with close-in Neptune- and Jupiter-mass planets.

This paper reports on a suite of follow-up observations of K2-25, a young M4.5 dwarf in the Hyades with a close-orbiting and transiting Neptune-sized planet. The new data allow us to measure the planet's mass and the star's obliquity. Section 2 introduces the K2-25 system. Section 3 presents the new photometric and spectroscopic observations. Section 4 describes the data reduction. Section 5 presents an updated determination of the stellar parameters, along with new estimates of the projected rotation velocity, rotation period, and stellar inclination with respect to the line of sight. Section 6 presents a joint analysis of the photometric and spectroscopic data and provides the results for the planet's mass and other system parameters. Section 7 focuses on the RM effect. All of the results are discussed in Section 8, along with the feasibility of future observations of the planet's transmission spectrum. We conclude with a summary of our key findings in Section 9.

2. The K2-25 System

The planet K2-25b was originally discovered by David et al. (2016) and Mann et al. (2016a) in data from the Kepler spacecraft as part of the K2 mission. It is a Neptune-sized planet ($R \sim 3.5\ R_{\oplus}$) in a $P = 3.5$ day orbit around its M4.5 dwarf host star in the Hyades. With its large transit depth of

1.1% and its brightness at near-infrared (NIR) wavelengths ($J = 11.3$), K2-25b has been discussed (see, e.g., David et al. 2016; Mann et al. 2016a) as a prime candidate for atmospheric characterization in the future with the James Webb Space Telescope (JWST), ARIEL (Tinetti et al. 2016), and large ground-based observatories. In addition, due to its large transit depth and the rapid stellar rotation ($P = 1.878$ days), K2-25b has an estimated RM effect amplitude of $\sim$60–70 m s^{-1}, making the RM effect detectable with high-precision RVs in the NIR. Further, planets with well-constrained ages are scarce, making the determination of K2-25b's 3D orbit valuable for constraining theories of planet formation and migration mechanisms that aim to explain planetary and orbital parameters as a function of age.

Recently, two groups discussed additional transit follow-up observations of K2-25b. Thao et al. (2020) studied the transit depth of K2-25b as a function of wavelength using photometric observations at different wavelengths from K2, the MEarth Observatories (Irwin et al. 2015), and the Las Cumbres Global Telescope Network (LCOGT) in the optical and the Spitzer Telescope in the NIR and found no significant evidence of changes in transit depth as a function of wavelength. To explain the flat broadband transmission spectrum, they favored a scenario where K2-25b has a cloudy atmosphere using a predicted mass from exoplanet mass–radius relations. Although K2-25 could have a cloudy atmosphere, we show in this paper that the apparent flat broadband transmission spectrum of K2-25b could also be partially explained by the larger observed mass of K2-25b than the mass assumed in Thao et al. (2020).

Kain et al. (2020) performed long-term photometric monitoring of K2-25 using the MEarth Observatories (Irwin et al. 2015) to monitor the activity of the star and look for evidence of transit timing variations (TTVs) in the transits of K2-25b, which could be suggestive of an additional planet orbiting in the system. They showed that the photometric variability of the star was significantly smaller between 2016 and 2018 than what K2 observed in its 71 day observing window in 2015. Kain et al. (2020) did not identify any definite starspot crossing events in their transit data, although a few of their transits could contain tentative evidence for such events. They further searched for TTVs in the system from the additional transits and found no evidence of significant TTVs, placing constraints on planetary companions orbiting close to the mean-motion resonances of K2-25b's orbit. This agrees with the transit observations presented in this work.

3. Observations

3.1. ARCTIC

We obtained five transits of K2-25b using the Astrophysical Research Consortium Telescope Imaging Camera (ARCTIC) imager (Huehnerhoff et al. 2016) on the 3.5 m Astrophysical Research Consortium (ARC) 3.5 m Telescope at Apache Point Observatory (APO) on the nights of UT 2017 September 17; 2019 January 4, 18, and 25; and 2019 February 1. All of the transit observations were performed with the Engineered Diffuser available on ARCTIC, which we designed specifically to enable very high precision photometric observations (see, e.g., Stefansson et al. 2017, 2018a, 2018b, 2020). We used the Sloan Digital Sky Survey (SDSS) i' filter, except on the night of 2019 January 18, when we used the SDSS z' filter without the diffuser to minimize background Moon contamination.

Table 1
Summary of Transit Observations Analyzed in This Work

Date (UT)	Instrument	Filter/Bandpass	Exposure Time (s)	Diffuser	Airmass Range	No. of Ref. Stars	Aperture Setting (pixels)
Photometric Transit Observations							
2018 Feb 7	HDI	SDSS z'	120	Yes	2.10, 1.16	9	21, 40, 60
2018 Feb 21	HDI	SDSS z'	120	Yes	1.84, 1.09	12	21, 40, 60
2018 Dec 14	HDI	SDSS z'	120	Yes	1.70, 1.04	7	22, 39, 59
2018 Dec 21	HDI	SDSS z'	30	No	1.37, 1.08	6	9, 16, 24
2017 Sep 17	ARCTIC	SDSS i'	20	Yes	1.68, 1.09	8	14, 35, 50
2019 Jan 4	ARCTIC	SDSS i'	30	Yes	1.41, 1.06	3	16, 28, 42
2019 Jan 18	ARCTIC	SDSS z'	30	No	1.23, 1.10	6	16, 50, 70
2019 Jan 25	ARCTIC	SDSS i'	30	Yes	1.34, 1.05	13	19, 30, 45
2019 Feb 1	ARCTIC	SDSS i'	30	Yes	1.11, 1.04	8	16, 28, 42
Spectroscopic Transit Observations							
2018 Dec 21	HPF	820–1280 nm	300	⋯	1.37, 1.17	⋯	⋯
2018 Dec 28	HPF	820–1280 nm	300	⋯	1.36, 1.17	⋯	⋯
2019 Jan 4	HPF	820–1280 nm	300	⋯	1.34, 1.18	⋯	⋯

Note. The Aperture Setting column lists the aperture setting in pixels used to extract the photometry in AstroImageJ (Collins et al. 2017), showing the radius of the photometric aperture and the radius of the inner and outer background annuli, respectively. The Airmass Range column shows the airmass range of the observations from high to low airmass. The observations on UT 2018 December 21 and UT 2019 January 18 were not performed with the diffuser due to the large Moon contamination on those nights.

Only the data from the egress from this night were usable due to the Moon contamination. The observations were performed in the quad readout and 4×4 binning mode, resulting in a readout time of 2.7 s. The first transit was observed with an exposure time of 20 s, and the rest of the transits were observed with an exposure time of 30 s. In this binning mode, ARCTIC has a gain of 2.0 e ADU^{-1} and a plate scale of $0\rlap{.}''44$ pixel^{-1}. Table 1 further summarizes the observations.

3.2. HDI

We observed four transits of K2-25b using the Half-Degree Imager (HDI; Deliyannis 2013) at the WIYN 0.9 m telescope at Kitt Peak National Observatory on the nights of UT 2018 February 7 and 21 and 2018 December 14 and 21. The HDI has a 4096×4096 pixel back-illuminated CCD from e2v, covering a $29\rlap{.}'2 \times 29\rlap{.}'2$ field of view (FOV) at a plate scale of $0\rlap{.}''425$ pixel^{-1}, with a gain of 1.3 e ADU^{-1} in the 1×1 binning mode. The observations were performed as part of the commissioning observations of the newly installed Engineered Diffuser for the telescope, which is now available for high-precision photometric observations. The Engineered Diffuser on HDI uses the same custom-optimized top-hat Engineered Diffuser pattern we developed for the ARC 3.5 m telescope with a diffuser opening angle of $\theta = 0\rlap{.}°34$ (Stefansson et al. 2017). The diffuser is placed in a filter wheel holder in the dual filter wheel 45 mm away from the focal plane, resulting in a stabilized point-spread function with an FWHM of $7\rlap{.}''6$. The size of the diffuser is 50.8×50.8 mm and vignettes the field to an effective FOV of $\sim 20' \times 20'$, still allowing for a number of available reference stars in the field.

Table 1 summarizes the observations and lists the number of reference stars and exposure time used. All of the observations were performed in the SDSS z' filter using the 1×1 binning mode. The first three observations were performed with the Engineered Diffuser with an exposure time of 120 s. The diffuser was not used on the night of 2018 December 21 due to the high degree of Moon contamination (the Moon was $\sim 97\%$ full and at a separation of $\sim 6°$ from the target). Further, during this night, we experienced issues with the camera shutter

causing the shutter to be stuck for periods of time, which led to gaps in the data stream seen in Figure 2(g). As the observations on that night were performed close to in focus, the exposure time used was scaled down to 30 s to minimize the risk of saturation. Two different readout modes were used for the observations: a quad readout mode and a single-amplifier readout mode, with readout times of 11 and 37 s, respectively. The observations on the nights of 2018 February 7 and December 21 used the single-amplifier readout mode, with the quad readout mode used for the other two.

3.3. HPF

We obtained precision NIR RVs of K2-25 with the Habitable Zone Planet Finder (HPF; Mahadevan et al. 2012, 2014) with the twofold goal to constrain the mass of K2-25b and the obliquity of the host star. The HPF is a high-resolution ($R \sim 55{,}000$) NIR fiber-fed spectrograph on the 10 m Hobby–Eberly Telescope (HET) at McDonald Observatory in Texas. It is actively temperature-stabilized to the millikelvin level to enable precision RVs in the NIR (Hearty et al. 2014; Stefansson et al. 2016). The HET is a fully queue-scheduled telescope with all observations executed in a queue by the HET resident astronomers (Shetrone et al. 2007). The HPF has an NIR laser-frequency comb (LFC) calibrator that has been shown to enable ~ 20 cm s^{-1} calibration precision and 1.5 m s^{-1} RV precision on-sky on the bright and stable M dwarf Barnard's Star (Metcalf et al. 2019).

In total, we obtained 105 spectra in 34 different visits with HPF. We removed 16 spectra after performing a signal-to-noise ratio (S/N) > 25 quality cut (S/N per pixel); these spectra were adversely affected by weather and deemed to be too low S/N. The median S/N of the 89 remaining spectra was 45, which was obtained in 32 different HET visits/tracks.[22]

For the out-of-transit observations, we obtained 69 spectra of K2-25b in 32 different tracks with HPF with a median S/N of 52 and median RV error bar of 42 m s^{-1}. For most of the

---

[22] The unique design of the HET only enables acquisition of K2-25 during a discrete east or west track with an ~ 1 hr maximum track duration.

spectra (58 in total), the exposure time was 969–1160 s, with two spectra obtained per HET visit. In addition to these spectra, we also use 11 spectra that were obtained during the out-of-transit baseline for the three transit observations described below. These spectra had an exposure time of 309 s and a median S/N of 32. To simplify the analysis and obtain the highest-precision error bar per RV visit, we performed a weighted average of the RVs of the out-of-transit RVs following the methodology described in Metcalf et al. (2019) and Stefansson et al. (2020). The final RVs used for the out-of-transit modeling are shown in Table C1 in Appendix C.

To constrain the obliquity of the K2-25b system, we obtained spectra of K2-25 during three transits on the nights of 2018 December 21 UT, 2018 December 28 UT, and 2019 January 4 UT. We used an exposure time of 309 s, corresponding to 29 up-the-ramp reads on the HPF Hawaii-2RG NIR detector, to obtain the required time resolution to resolve the RM waveform. Overall, we obtained 11, 11, and 9 spectra in the three different visits, respectively. The three sets of spectra had median S/Ns of 33, 36, and 35 (per extracted 1D pixel) and median RV errors of 85, 72, and 74 m s^{-1}, respectively. Out of these 31 spectra, 20 were in transit and 11 out of transit. The S/N of the first night (2018 December 21 UT) was the lowest, as the Moon was $\sim$97% full and only $\sim$6° away from the target during the observations. Making the S/N > 25 quality cut described above removed one out-of-transit baseline spectrum that was observed at the edge of the available HET track during the transit on 2019 January 4 UT. Table 1 further summarizes the in-transit observations. The final RVs used for the in-transit modeling are shown in Table C2 in Appendix C.

Following our observational setup, described in Stefansson et al. (2020), due to the faintness of the target ($J = 11.3$), we elected not to have the HPF LFC on for any of the observations described, to minimize the risk that the bright LFC lines would contaminate the stellar spectrum. This does not significantly impact the drift correction for this target, as the drift of HPF is linear during a night (amplitude of $\sim$10 m s^{-1}) and well traced and calibrated to <1 m s^{-1} RV precision by daily HPF calibrations and a linear drift model, as has been detailed in Stefansson et al. (2020). For all of the observations above, the HPF sky fiber was used to subtract any Moon and/or other sources of background light contamination.

4. Data Reduction

4.1. Photometric Observations

We reduced the photometry using AstroImageJ (Collins et al. 2017), following a similar methodology as in Stefansson et al. (2017, 2018a). In short, we experimented using a number of different aperture settings, varying the radii of the software aperture and inner and outer background annuli and selecting the aperture setting that resulted in the minimum rms scatter in the resulting photometry. Table 1 summarizes the aperture setting used for each observation in pixels that led to the lowest photometric noise in the light curve. We add the scintillation error bar estimates to the photometric error bars estimated by AstroImageJ following the methodology in Stefansson et al. (2017). The individual exposures were calibrated using standard median bias, dark, and flat-field procedures in AstroImageJ following Stefansson et al. (2017). The median bias, dark, and flat-field exposures were taken at the beginning

or end of each night of observation. We converted the time stamps of the ground-based observations to Barycentric Julian Date time (BJD$_{\mathrm{TDB}}$) using the Python package `barycorrpy` (Kanodia & Wright 2018), which uses the barycentric correction algorithm from Wright & Eastman (2014).

From 2015 February 8 to April 20, K2-25b was observed by the K2 mission as part of Campaign 4 in long-cadence (30 minute exposures) mode, resulting in 71 days of continuous photometric observations. We use the light curve from the `Everest` pipeline (Luger et al. 2016), which is capable of correcting the periodic correlated errors in the K2 data due to imperfect pointing of the spacecraft. The corrected `Everest` light curve improved the 6 hr CDPP standard deviation of the raw K2 long-cadence data of K2-25 from 432 to 295 ppm.

4.2. Spectroscopic Observations

The HPF 1D spectra were reduced and extracted with the custom HPF data extraction pipeline following the procedures outlined in Ninan et al. (2018), Kaplan et al. (2018), and Metcalf et al. (2019). For the RV extractions, we used the Spectrum Radial Velocity Analyzer (SERVAL), which we have adapted for use for the HPF spectra, following the methodology described in Metcalf et al. (2019) and Stefansson et al. (2020). In short, SERVAL uses the template-matching method to measure the RVs (see, e.g., Anglada-Escudé & Butler 2012; Zechmeister et al. 2018). We extracted the HPF RVs using the eight orders with the least telluric contamination in the HPF bandpass (orders covering the wavelength regions from 8540 to 8890 and 9940 to 10760 Å). Although we plan to include more orders in the RV extraction to potentially enable even higher RV precision, we elected to use only these eight orders that we have extensively tested to produce reliable RVs with HPF. We subtracted the estimated sky background from the stellar spectrum using the dedicated HPF sky fiber. Following the methodology described in Metcalf et al. (2019), we explicitly masked out telluric and sky emission lines to minimize their impact on the RV determination. To minimize the impact of the asymmetric spectral line variations seen during the RM effect, we generated the master RV template to extract the RV using only out-of-transit spectra. As described in Section 3.3, this resulted in 40 spectra after a quality cut of S/N > 25 used to generate the master RV template.

We calculated the RVs in two steps. First, to generate a first-pass master template, we ignored any possible planetary-induced RVs and coadded the out-of-transit spectra (after barycentric correction) using the SERVAL template creation functionality, which we then used to derive a first set of RVs. We then used this first set of RVs to further align the out-of-transit spectra to create a second-pass RV template and reextracted the RVs using this more refined template. The out-of-transit RVs used for the mass determination of K2-25b are shown in Table C1 in Appendix C, and the in-transit RVs are shown in Table C2.

5. Stellar Parameters

The stellar parameters used in this work are summarized in Table 2 and are broadly adopted from the values presented in Mann et al. (2016a) and Thao et al. (2020). Thao et al. (2020) estimated their stellar parameters (including the stellar radius and mass) using the empirically calibrated relations of

Table 2
Summary of Stellar Parameters Used in This Work

Parameter	Description	Value	References
Main Identifiers			
EPIC	…	210490365	Huber
Stellar Magnitudes			
B	APASS Johnson B mag	17.449 ± 0.144	APASS
V	APASS Johnson V mag	15.891 ± 0.180	APASS
g'	APASS Sloan g' mag	16.567 ± 0.018	APASS
r'	APASS Sloan r' mag	15.300 ± 0.183	APASS
i'	APASS Sloan i' mag	13.698 ± 0.206	APASS
Kepler-mag	Kepler magnitude	14.528	Huber
J	2MASS J mag	11.303 ± 0.021	2MASS
H	2MASS H mag	10.732 ± 0.020	2MASS
K_S	2MASS K_S mag	10.444 ± 0.019	2MASS
WISE1	WISE1 mag	10.275 ± 0.024	WISE
WISE2	WISE2 mag	10.086 ± 0.020	WISE
WISE3	WISE3 mag	9.936 ± 0.057	WISE
Stellar Parameters			
M_*	Mass in $M_\odot$	0.2634 ± 0.0077	Thao et al. (2020)
R_*	Radius in $R_\odot$	0.2932 ± 0.0093	Thao et al. (2020)
ρ_*	Density in g cm^{-3}	14.7 ± 1.5	Thao et al. (2020)
$\log(g)$	Surface gravity in cgs units	4.944 ± 0.031	Derived from M and R
T_{eff}	Effective temperature in K	3207 ± 58	Thao et al. (2020)
[Fe/H]	Metallicity in dex	0.15 ± 0.03	Mann et al. (2016a)
Age	Age in Gyr	$0.730^{+0.050}_{-0.052}$	Mann et al. (2016a)
L_*	Luminosity in $L_\odot$	0.00816 ± 0.00029	Thao et al. (2020)
d	Distance in pc	$45.01^{+0.16}_{-0.17}$	Gaia
π	Parallax in mas	$22.218^{+0.081}_{-0.083}$	Gaia
P_{rot}	Rotational period in days	1.878 ± 0.005	This work
$v \sin i_*$	Stellar rotational velocity in km s^{-1}	8.8 ± 0.6	This work
i_*	Stellar inclination	$90° \pm 12°$	This work

References. Huber (Huber et al. 2016), Lepine (Lépine & Shara 2005), Reid (Reid et al. 2004), Gaia (Gaia Collaboration 2018), APASS (Henden et al. 2015), UCAC2 (Zacharias et al. 2004), 2MASS (Cutri et al. 2003), WISE (Cutri et al. 2014).

Mann et al. (2015, 2019). As an additional test of these parameters, we performed an independent spectral energy distribution (SED) and isochrone fit using the EXOFASTv2 package (Eastman 2017; Eastman et al. 2019), placing informative Gaussian priors on the known metallicity ([Fe/H] = 0.15 ± 0.03) and age (age = 730 ± 50 Myr) of the star derived from its Hyades cluster membership (Mann et al. 2016a), along with its known distance from Gaia. The values we obtained are in good agreement with the values from Thao et al. (2020), in particular, obtaining a fully consistent stellar density value from the stellar mass and radius (we obtain a density of $\rho = 14.7 \pm 1.2$ g cm^{-3}, and they obtain $\rho = 14.7 \pm 1.5$ g cm^{-3}), which carries important information on the eccentricity of the planet via the photoeccentric effect (see, e.g., Dawson & Johnson 2012). We elected to incorporate the values from Thao et al. (2020) for our analysis, as they are derived from precise empirically calibrated relations, rather than through model-dependent SED and isochrone fitting. We note that with an effective temperature of $T_{\mathrm{eff}} = 3207$ K and radius of $R = 0.29 R_\oplus$, K2-25 lies at the higher-radius end of the radius discontinuity for low-mass M dwarfs in Rabus et al. (2019), which they observe for M dwarfs with effective temperatures between 3200 and 3300 K. This radius discontinuity has been interpreted as the boundary between partially and fully convective M dwarfs, and as K2-25 is observed to be just above the radius discontinuity, it suggests that K2-25 is potentially partially convective and just at the onset of being a fully convective star. Our estimate of the stellar rotation period, projected rotational velocity, and stellar inclination are discussed in the next two subsections.

5.1. Rotation Period

The K2 data of K2-25b are modulated at the 1% level, suggestive of starspots and/or active regions that rotate in and out of view with the rotation period of the star. We independently measure the rotation period of K2-25b following the methodology in Stefansson et al. (2020). In short, we model the stellar active regions using a quasiperiodic Gaussian process (GP), as quasiperiodic GP kernels have been shown to yield reliable stellar rotation rates (Angus et al. 2018). For computational efficiency, we adopt the quasiperiodic kernel from the celerite package (Foreman-Mackey et al. 2017) as implemented in juliet. The form of this kernel is further discussed in Section 6.1. To estimate the rotation period, we removed points within windows that were twice the transit duration in length centered around the transit midpoints and fit the resulting photometry using the celerite quasiperiodic GP kernel (see Foreman-Mackey et al. 2017 and Equation (3) in Section 6.1). We placed noninformative priors on the GP period, amplitude, and GP decay timescale parameters.

Figure 1 shows the resulting posteriors of the GP period hyperparameter along with the phase-folded photometry using our best-fit rotation period of $P_{\mathrm{rot}} = 1.878 \pm 0.005$ days. In the phase-folded photometry, we see that the photometric modulation remains relatively stable throughout the 71 days of the K2
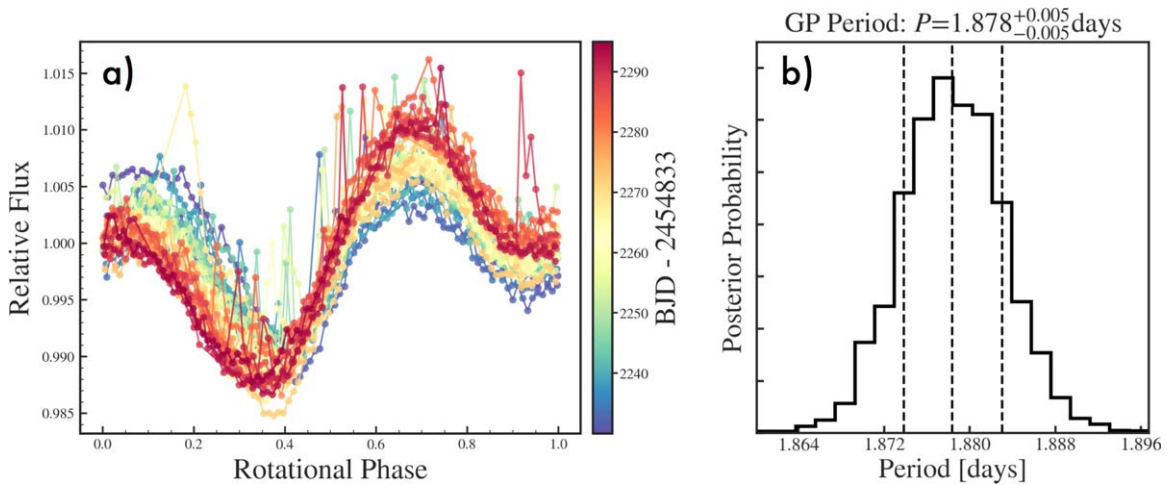
Figure 1. (a) Phase-folded K2 photometry of K2-25 using our best estimate of the rotation period (see panel (b)), showing a clear periodic photometric modulation. The photometric modulation remains stable over the 71 day K2 photometric baseline, with a slight evolution. (b) Posteriors of the period of the quasiperiodic GP kernel, which we interpret as the stellar rotation period.

data set, with a slight evolution. From Figure 1, we also see evidence of flares. Our period estimate agrees well with the rotation period reported in Mann et al. (2016a) of $P_{\rm rot} = 1.881 \pm 0.021$ days estimated using an autocorrelation function method and Dmitrienko & Savanov (2017) of $P_{\rm rot} = 1.878 \pm 0.030$ days from power-spectrum analysis. The top panel of Figure 2 in Section 6 shows the modulation in the K2 photometry as a function of time for the full 71 day baseline.

5.2. Projected Rotational Velocity and Stellar Inclination

We measured the projected rotational velocity using the empirical spectral matching algorithm described in Stefansson et al. (2020), which closely follows the `SpecMatchEmp` algorithm described in Yee et al. (2017). In short, the algorithm compares the observed target star spectrum to a library of observed slowly rotating stellar spectra using a χ^2 metric, and we refer the reader to Stefansson et al. (2020) for a more detailed discussion.

We used the algorithm to measure independent $v \sin i_*$ values for the eight HPF orders cleanest of tellurics. Table 3 shows the resulting values, showing that the independent orders agree well on the resulting value, with a mean value of $v \sin i_* = 8.8$ km s^{-1} and a scatter of 0.3 km s^{-1}. The values in Table 3 show a small formal scatter at the 0.3 km s^{-1} level. However, given our experience calculating the $v \sin i_*$ values of other stars from high-resolution spectra with HPF, a more realistic error estimate is a factor of 2 larger. We adopt an error estimate of 0.6 km s^{-1} to account for possible systematics in our method, as $v \sin i_*$ measurements are generally dominated by systematics (see, e.g., Reiners et al. 2012). As such, we adopt a $v \sin i_* = 8.8 \pm 0.6$ km s^{-1}. We note that value is somewhat larger than the value presented in Mann et al. (2016a) of $v \sin i_* = 7.8 \pm 0.5$ km s^{-1}, determined from their observed spectra obtained with the IGRINS spectrograph. The method used in Mann et al. (2016a) used an overall similar χ^2 method as presented here but used artificially rotationally broadened theoretical BT-SETTL spectra for the χ^2 comparison instead of observed spectra. Although this value is formally slightly higher than the maximum equatorial velocity of the star of 7.9 ± 0.25 km s^{-1} (assuming a stellar radius of

$R = 0.2932 \pm 0.0093$ $R_\odot$ and stellar rotation period of $P = 1.878 \pm 0.005$ days), the two values overlap within the 2σ uncertainties. The high $v \sin i_*$ suggests that the stellar inclination is close to 90°.

To estimate accurate posteriors for the stellar inclination i_* from the stellar rotational velocity v estimated from R and $P_{\rm rot}$ and its sky projection $v \sin i_*$ measured from the HPF spectra, we use the formalism in Masuda & Winn (2020), which accurately accounts for the correlated dependence between $v \sin i_*$ and v. The $v \sin i_*$ measurement does not distinguish between solutions between i and $180° - i$, and we thus calculate two independent solutions between 0° and 90° and 90° and 180°, respectively. Using the values listed in Table 2 for $P_{\rm rot}$, $v \sin i_*$, and R, we obtain two mirrored posteriors with a highest-likelihood inclination at 90°. Taken together, the two solutions result in an inclination constraint of $90° \pm 12°$, consistent with viewing K2-25's stellar equator edge-on. This agrees well with the stellar inclination constraint provided by Mann et al. (2016a) of $i_* > 79°$ at 1σ (68.4% confidence; they considered inclinations between 0° and 90°).

6. Planet Parameters from Transit Photometry and RVs

6.1. Transit, RV, and GP Models

We jointly model the K2 and ground-based transits and the HPF out-of-transit RVs using the `juliet` Python package (Espinoza et al. 2019), which uses the `batman` Python package (Kreidberg 2015) for the transit model and the `radvel` package (Fulton et al. 2018) for the RV model. We used the `dynesty` sampler (Speagle 2020) available in `juliet` to perform dynamic nested sampling to obtain both posterior and evidence estimates, where we used the default weight and stopping functions and stopping criteria in `dynesty`.[23] The total log-likelihood in `juliet` is the sum of the individual log-likelihoods of each data set considered.[24]

Following the implementation in `juliet`, we parameterize the radius ratio $p = R_p/R_*$ and the impact parameter b using

---

[23] For a description of the weight and stopping functions in the dynamic nested sampler in `dynesty`, see Section 3 in Speagle (2020).

[24] See equations and discussion surrounding Equations (6) and (7) in Espinoza et al. (2019) to see the explicit likelihood used in `juliet`.
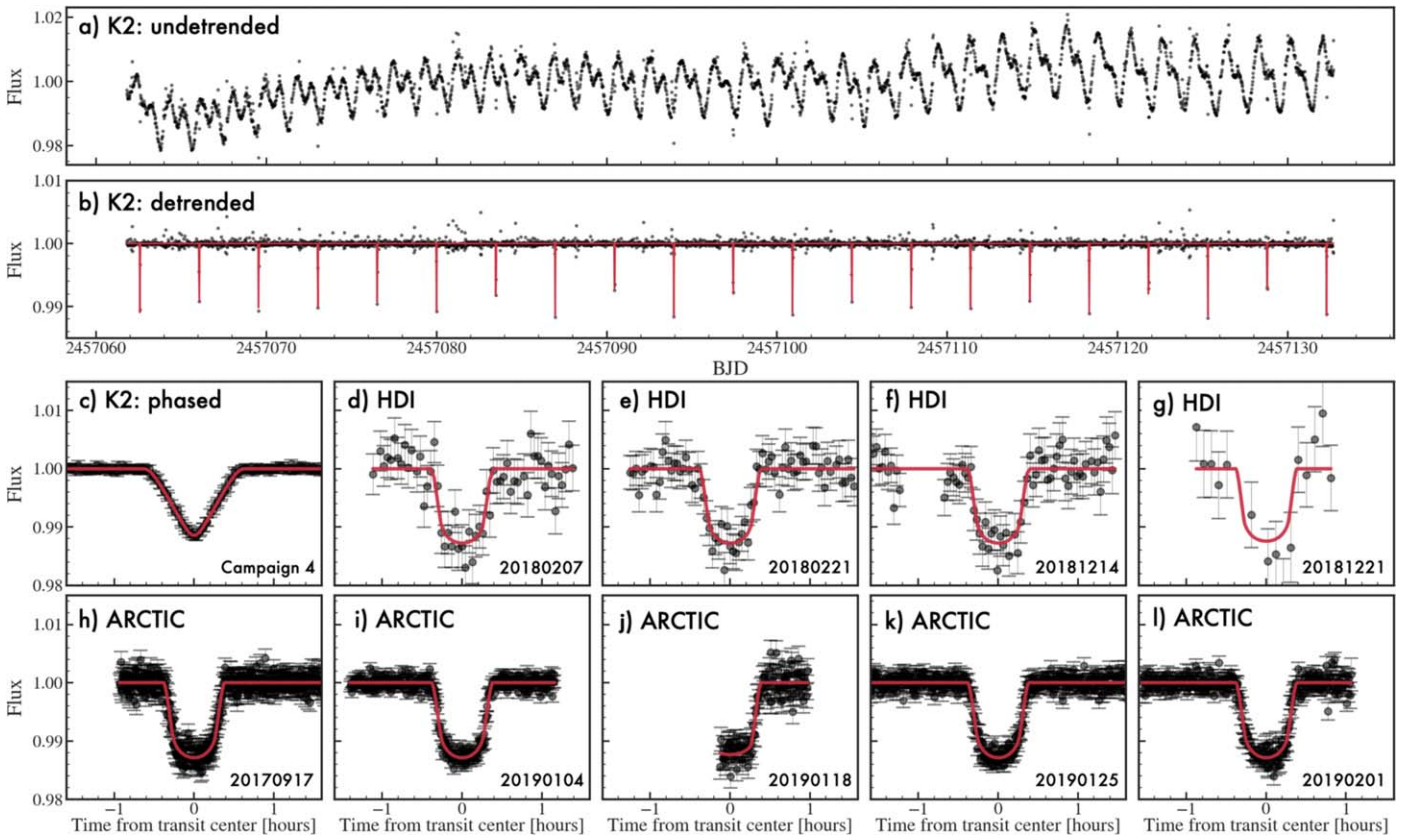
Figure 2. (a) K2 light curve of K2-25 corrected for instrument systematics using the `Everest` pipeline, showing clear starspot-induced rotational modulations. (b) Detrended and flattened K2 light curve (black points) using the best-fit GP model from model RV2 in Table 5, along with the best-fit transit model from `Juliet` (shown in red). (c) Phased K2 light curve (black) along with the best-fit transit model (red). (d)–(g) Ground-based transits as observed with HDI showing the best-fit transit model from `Juliet` in red. We note that the HDI transit on 2018 December 21 (panel (g)) was observed without the diffuser during suboptimal observing conditions (Moon illumination 97%). Although the light curve was modeled unbinned, it is shown here binned to a cadence of ∼6 minutes for clarity. (h)–(l) Ground-based transits observed with the 3.5 m ARC telescope at APO. All of the ARCTIC observations were observed using a diffuser, except the transit on the night of 2019 January 18 UT (panel (j)).

(The data used to create this figure are available.)

Table 3
Resulting $v \sin i_*$ Values for the Eight Different HPF Orders Cleanest of Tellurics

Order	Wavelength Region (Å)	$v \sin i_*$ (km s^{-1})
4	[8540, 8640]	8.3
5	[8670, 8750]	8.9
6	[8790, 8885]	8.6
14	[9940, 10055]	8.8
15	[10105, 10220]	8.8
16	[10280, 10395]	9.0
17	[10460, 10570]	9.3
18	[10640, 10760]	8.9

Note. The resulting median value is $v \sin i_* = 8.8$ km s^{-1} with a scatter of 0.3 km s^{-1}. As mentioned in the text, we adopt a value of $v \sin i_* = 8.8 \pm 0.6$ km s^{-1}.

the efficient r_1 and r_2 parameterization described in Espinoza (2018). We sampled the limb-darkening parameters using the quadratic q_1 and q_2 limb-darkening parameterization from Kipping (2013). Following the suggestion in Kipping (2010), we resampled and rebinned our transit model to the effective 30 minute exposure time of the long-cadence K2 data to account for the smoothing of the transit shape. We assumed

that there was no source of dilution, as no obvious close-by companion is seen in the adaptive optics imaging presented in Mann et al. (2016a).

We used a GP model with three different kernels to account for the characteristic correlated noise behavior in the K2 photometry, ground-based photometry, and RVs. The GPs have been used by a number of groups to jointly model correlated noise observed in photometric and RV data due to stellar active regions on the surface of the star (e.g., spots, faculae, and plages; see, e.g., Haywood et al. 2014, 2018; Grunblatt et al. 2015; López-Morales et al. 2016; Dai et al. 2017; Angus et al. 2018). For our GP modeling, we use the GP kernels available in `juliet`, which are based on the GP implementations from the `george` (Ambikasaran et al. 2015) and `celerite` (Foreman-Mackey et al. 2017) Python packages. In `juliet`, the elements of the covariance matrix C_i for instrument i are assumed to be of the form

$$C_{i,l,m} = k_i(x_l, x_m) + (\sigma_{i,w}^2 + \sigma_{t_l,i}^2)\delta_{l,m}, \qquad (1)$$

where $\delta_{l,m}$ is the Kronecker delta function, $k_i(x_l, x_m)$ is the kernel of the GP for instrument i, $\sigma_{t_l,i}$ is the error estimated at time t_l, and $\sigma_{i,w}$ is an additional white-noise jitter parameter. For all of the GP fits considered, we fit a kernel function, as

well as a separate white-noise jitter term for each instrument, as is shown in Equation (1).

We choose three different GP kernels as a balance between computational speed and adequately accounting for the characteristic correlated noise properties of the different data sets. First, to model the correlated noise in the RV observations, we elect to use the quasiperiodic rotational kernel, which has been shown to be effective at modeling rotational variations in RV data sets and has well-studied hyperparameters (Haywood et al. 2014, 2018; Grunblatt et al. 2015). In `juliet`, the quasiperiodic kernel is given with the form

$$k(x_l, x_m) = \sigma_{\mathrm{GP}}^2 \exp\left(-\alpha\tau^2 - \Gamma \sin^2\left[\frac{\pi\tau}{P_{\mathrm{GP}}}\right]\right), \qquad (2)$$

where $\tau = |x_l - x_m|$, with hyperparameters σ_{GP} (RV amplitude in m s^{-1}), α (inverse square timescale in units of day^{-2}), Γ (a unitless scaling parameter), and P_{GP} (the periodicity of the GP in days, which we interpret as the rotation period).[25] The Γ parameter changes the amplitude of the sin^2 term and controls the harmonic structure of the resulting GP model (see, e.g., discussion in Angus et al. 2018). We follow Haywood et al. (2018) and place an informative prior on the Γ parameter; Haywood et al. (2018) placed an informative Gaussian prior of $\eta_4 = 0.5 \pm 0.05$, which corresponds to $\Gamma = 8 \pm 1.9$ (in their notation, $\Gamma = 2/\eta_4^2$). Doing so causes the RV curve to have up to two or three maxima and two or three minima per rotation, as is typical of stellar light curves and RV curves (Haywood et al. 2018).

Second, for a computationally efficient analysis of the K2 data, we elect to use the quasiperiodic kernel available in `celerite` (Foreman-Mackey et al. 2017), where the kernel function is given with the form

$$k(x_l, x_m) = \frac{B}{2+C} e^{-\tau/L}\left[\cos\left(\frac{2\pi\tau}{P_{\mathrm{GP}}}\right) + (1+C)\right], \qquad (3)$$

where $\tau = |x_l - x_m|$, and B, C, L, and P_{rot} are the hyperparameters of the kernel. Here B and C tune the weight of the exponential decay component of the kernel with a decay constant of L (in days), and P_{GP} corresponds to the periodicity of the quasiperiodic oscillations, which we interpret as the stellar rotation period. Although not exactly of the same form as the kernel in Equation (2), we selected this kernel, as it shares similar quasiperiodic properties as the kernel in Equation (2) but is orders of magnitude faster to evaluate on the large number of K2 data points (see discussion in Foreman-Mackey et al. 2017). Given the high precision and clear photometric modulation seen in the K2 data, we shared the P_{GP} parameter between the quasiperiodic K2 GP kernel and our quasiperiodic RV kernel to allow the high-precision K2 photometry to accurately constrain the P_{GP} parameter. We did not share any other GP parameters between the K2 and RV kernels, given the different forms of the kernels used. Table 4 further lists all of the priors used and which parameters are linked between different GP kernels.

Lastly, the ground-based photometric transit observations are not long enough to be measurably impacted by the starspot modulation seen in the K2 light curve. Instead, the characteristic timescales of the observed correlated noise are much shorter or <1 hr, originating from observational and/or instrumental systematics. Therefore, for the ground-based observations, we adopt the approximate Matern 3/2 kernel multiplied by an exponential kernel that has covariance properties that are better matched to these timescales (see, e.g., Pepper et al. 2017; Espinoza et al. 2019). As implemented in `juliet`, this kernel has the form (see also Foreman-Mackey et al. 2017)

$$k(x_l, x_m) = \sigma_{\mathrm{GP}}^2 e^{-\tau/L}[(1+1/\epsilon)e^{-1(1-\epsilon)s} \\ + (1-1/\epsilon)e^{-1(1+\epsilon)s}], \qquad (4)$$

where $s = \sqrt{3}\,\tau/\rho$ and $\tau = |x_l - x_m|$, with hyperparameters σ_{GP} (photometric amplitude in ppm), L (length scale of the exponential component in days), and ρ (length scale of the Matern 3/2 kernel in days) and $\epsilon = 0.01$, where we note that as ϵ approaches zero, the factor inside the brackets converges to a Matern 3/2 kernel (Foreman-Mackey et al. 2017; Espinoza et al. 2019). To allow for sufficient flexibility in modeling out different systematics seen in the different observing setups in the ground-based light curves, we assigned each ground-based transit an independent approximate Matern 3/2 kernel with independent hyperparameters (σ_{GP}, L, and ρ). As an additional test, we also experimented using a pure exponential kernel to model the correlations seen in the ground-based data (with a timescale L and σ amplitude parameters) as implemented in `juliet`. Although both kernels yielded consistent planet parameters within the 68.3% credible intervals of the posteriors ($\sim 1\sigma$ uncertainties for a Gaussian distribution) in our experiments, the pure exponential kernel tended to favor small decay values that visually overfit the noise structures in the data. The additional capability of the composite kernel in Equation (4) to account for both lower- and higher-frequency-correlated noise in the ground-based light curves led to less overfitting of the noise (see, e.g., additional discussions in Pepper et al. 2017; Espinoza et al. 2019), and we thus favor this kernel in our analysis.

To investigate the evidence for eccentricity in the system and study the impact that our GP RV model has on the derived orbital parameters, we ran three different models. First, we performed a fit assuming a circular orbit ($e = 0$; model RV1 in Table 4) with a simultaneous GP fit for the transits and RV data. Second, we performed a fit letting the eccentricity e and argument of periastron ω float (model RV2 in Table 4) while also performing a simultaneous GP fit like in model RV1. Third, we let e and ω float but removed the GP model on the RV data (keeping the GP model for the photometry; model RV3 in Table 4). The priors for these three models are summarized in Table 4. In total, we sampled 70, 72, and 69 parameters for the three fits, where we obtained 64,077, 54,258, and 52,522 posterior samples for the three models, respectively.

In all three models, we place a Gaussian prior on the stellar density of $\rho = 14.7 \pm 1.5$ g cm^{-3} estimated from the mass and radius of the star in Table 2. Doing so allows us to place an important constraint on the eccentricity and argument of periastron derived from the transit from the photoeccentric

---

[25] As mentioned by Espinoza et al. (2019), the hyperparameters in Equation (2) correspond to the following parameters in the notation of Haywood et al. (2018): $\sigma_{\mathrm{GP}} = \eta_1$, $\alpha = 1/2\eta_2^2$, $P_{\mathrm{rot}} = \eta_3$, and $\Gamma = 2/\eta_4^2$.

Table 4
Summary of Priors Used for the Three Joint Transit and RV Fits Performed

Parameter	Description	Model RV1 $(e = 0,$ GP for RVs)	Model RV2 $(e \neq 0,$ GP for RVs)	Model RV3 $(e \neq 0,$ No GP for RVs)
Orbital Parameters				
P (days)	Orbital period	$\mathcal{N}(3.484{,}548, 0.000{,}042)$	$\mathcal{N}(3.484{,}548, 0.000{,}042)$	$\mathcal{N}(3.484{,}548, 0.000{,}042)$
T_C	Transit midpoint–2,400,000 (BJD$_{\rm TDB}$)	$\mathcal{U}(58{,}515.63, 58{,}515.66)$	$\mathcal{U}(58{,}515.63, 58{,}515.66)$	$\mathcal{U}(58{,}515.63, 58{,}515.66)$
r_1[a]	Radius ratio/impact parameter	$\mathcal{U}(0, 1)$	$\mathcal{U}(0, 1)$	$\mathcal{U}(0, 1)$
r_2[a]	Radius ratio/impact parameter	$\mathcal{U}(0, 1)$	$\mathcal{U}(0, 1)$	$\mathcal{U}(0, 1)$
a/R_*	Scaled semimajor axis	$\mathcal{U}(1, 50)$	$\mathcal{U}(1, 50)$	$\mathcal{U}(1, 50)$
$m_{\rm flux}$	Transit baseline parameter	$\mathcal{U}(0, 0.1)$	$\mathcal{U}(0, 0.1)$	$\mathcal{U}(0, 0.1)$
$\sigma_{\rm K2}$	Photometric error bar (ppm)	$\mathcal{J}(1, 1000)$	$\mathcal{J}(1, 1000)$	$\mathcal{J}(1, 1000)$
e	Eccentricity	0 (fixed)	$\mathcal{U}(0, 0.95)$	$\mathcal{U}(0, 0.95)$
ω	Argument of periastron	90 (fixed)	$\mathcal{U}(0, 360)$	$\mathcal{U}(0, 360)$
K	RV semiamplitude (m s^{-1})	$\mathcal{U}(0, 200)$	$\mathcal{U}(0, 200)$	$\mathcal{U}(0, 200)$
Other Constraints				
ρ_*	Stellar density (g cm^{-3})	$\mathcal{N}(14.7, 1.5)$	$\mathcal{N}(14.7, 1.5)$	$\mathcal{N}(14.7, 1.5)$
Jitter and Other Instrumental Terms				
q_1[b]	Limb-darkening parameter	$\mathcal{U}(0, 1)$	$\mathcal{U}(0, 1)$	$\mathcal{U}(0, 1)$
q_2[b]	Limb-darkening parameter	$\mathcal{U}(0, 1)$	$\mathcal{U}(0, 1)$	$\mathcal{U}(0, 1)$
$\sigma_{\rm phot}$[c]	Photometric jitter (ppm)	$\mathcal{J}(1, 1000)$	$\mathcal{J}(1, 1000)$	$\mathcal{J}(1, 1000)$
$\mu_{\rm phot}$[c]	Photometric baseline	$\mathcal{N}(0, 0.1)$	$\mathcal{N}(0, 0.1)$	$\mathcal{N}(0, 0.1)$
$\sigma_{\rm HPF}$	HPF RV jitter (m s^{-1})	$\mathcal{J}(0.1, 300)$	$\mathcal{J}(0.1, 300)$	$\mathcal{J}(0.1, 300)$
$\mu_{\rm HPF}$	HPF RV offset (m s^{-1})	$\mathcal{U}(-200, 200)$	$\mathcal{U}(-200, 200)$	$\mathcal{U}(-200, 200)$
Shared Photometric and RV Quasiperiodic GP Parameters				
$P_{\rm GP}$	GP period (days)	$\mathcal{N}(1.8{,}784, 0.005)$	$\mathcal{N}(1.8{,}784, 0.005)$	$\mathcal{N}(1.8{,}784, 0.005)$
K2 Quasiperiodic GP Parameters				
B	Photometric GP amplitude (ppm^2)	$\mathcal{J}(10^{-6}, 10^5)$	$\mathcal{J}(10^{-6}, 10^5)$	$\mathcal{J}(10^{-6}, 10^5)$
C	GP additive factor	$\mathcal{J}(10^{-6}, 10^5)$	$\mathcal{J}(10^{-6}, 10^5)$	$\mathcal{J}(10^{-6}, 10^5)$
L	GP length scale (days)	$\mathcal{J}(10^3, 10^6)$	$\mathcal{J}(10^3, 10^6)$	$\mathcal{J}(10^3, 10^6)$
Ground-based Approximate Matern GP Parameters[d]				
$\sigma_{\rm GP}$	Photometric GP amplitude (ppm)	$\mathcal{J}(10^{-1}, 10^4)$	$\mathcal{J}(10^{-1}, 10^4)$	$\mathcal{J}(10^{-1}, 10^4)$
L	Timescale of exponential kernel (days)	$\mathcal{J}(10^{-2}, 10^5)$	$\mathcal{J}(10^{-2}, 10^5)$	$\mathcal{J}(10^{-2}, 10^5)$
ρ	Timescale of Matern kernel (days)	$\mathcal{J}(10^{-2}, 10^5)$	$\mathcal{J}(10^{-2}, 10^5)$	$\mathcal{J}(10^{-2}, 10^5)$
RV GP Parameters				
$\sigma_{\rm GP}$	RV GP amplitude (m s^{-1})	$\mathcal{J}(10^1, 10^5)$	$\mathcal{U}(10^1, 10^5)$	⋯
Γ	Harmonic structure/scaling parameter	$\mathcal{N}(8.0, 1.9)$	$\mathcal{N}(8.0, 1.9)$	⋯
α	Inverse length scale (day^{-2})	$\mathcal{J}(10^{-12}, 10^{-3})$	$\mathcal{J}(10^{-12}, 10^{-3})$	⋯

Notes. Here $\mathcal{N}(m, \sigma)$ denotes a normal prior with mean m and standard deviation σ, $\mathcal{U}(a, b)$ denotes a uniform prior with a start value a and end value b, and $\mathcal{J}(a, b)$ denotes a Jeffreys prior with a start value a and end value b. A Gaussian prior on the stellar density was placed for all fits. The dilution parameters in `juliet` were fixed to 1 for all transit observations. For the three models considered, we sampled 70, 72, and 69 parameters.
[a] Using the efficient sampling of the r_1 and r_2 parameterization for the impact parameter b and radius ratio $p = R_p/R_*$ as described in Espinoza (2018).
[b] Overall, we modeled four pairs of limb-darkening parameters q_1 and q_2 (parameterization from Kipping 2013): (a) one pair for K2, (b) one pair for all of the transits observed with ARCTIC in the SDSS i' filter, (c) one pair for the ARCTIC SDSS z' filter observations, and (d) one pair for the HDI transits in the SDSS z' filter.
[c] We placed a separate photometric jitter term and baseline offset term for each of the photometric observations.
[d] We placed one set of three parameters ($\sigma_{\rm GP}$, L, ρ) for each of the ground-based transits.

effect (Dawson & Johnson 2012). Mann et al. (2016a) and Thao et al. (2020) also reported evidence of nonzero eccentricity in the system from their analyses of $e = 0.27^{+0.16}_{-0.21}$ and $e = 0.27^{+0.16}_{-0.06}$, respectively. Our data also favor an eccentric solution. In performing a circular fit placing no constraint on the stellar density, the resulting best fit yielded a stellar density of $\rho = 40 \pm 4$ g cm^{-3}, significantly larger than the expected stellar density of $\rho = 14.7 \pm 1.5$ g cm^{-3}. Therefore, to ensure an a/R_* value that results in a stellar density consistent with our estimated stellar density derived from the star's mass and radius, we placed an informative Gaussian prior on the stellar density in all fits reported in Table 5.

To estimate the expected photometric amplitude from ellipsoidal variations caused by tidal interactions between the planet and the host star, we used Equation (7) in Shporer (2017), which gives the expected ellipsoidal variation amplitude in ppm as a function of the stellar mass, planetary mass, orbital distance of the planet, and limb- and gravity-darkening parameters of the host star. Using our parameter constraints and nominal vales for the limb- and gravity-darkening parameters and assuming a circular orbit with $a/R_* = 21$, we obtain an expected ellipsoidal variation amplitude of 0.03 ppm. Even if we assume a circular orbit at K2-25b's periastron distance of $a/R_* \sim 11.5$, we obtain a small expected ellipsoidal variation amplitude of 0.2 ppm. Both values are substantially below the photometric precision of our data sets. Given the low amplitude of the signal, we did not attempt to fit any ellipsoidal variations as part of our transit model.

Table 5
Median Values and 68% Credible Intervals for the Three Joint-fit Models Considered

Parameter	Description	Model RV1 (e = 0, with GP for RVs)	**Model RV2 (Adopted)** (e ≠ 0, with GP for RVs)	Model RV3 (e ≠ 0, No GP for RVs)
Model Evidence				
$\ln Z$	Model log evidence	$25{,}828.7 \pm 9.9$	$25{,}875.4 \pm 4.1$	$25{,}869.9 \pm 4.2$
Planet Parameters				
T_C (BJD$_{\rm TDB}$)	Transit midpoint	$2458515.64215^{+0.00008}_{-0.00008}$	$2458515.64206^{+0.00010}_{-0.00009}$	$2458515.642134^{+0.00008}_{-0.00008}$
P	Orbital period (days)	$3.48456408^{+0.0000005}_{-0.0000005}$	$3.48456408^{+0.0000006}_{-0.0000006}$	$3.48456407^{+0.0000005}_{-0.0000006}$
(R_p/R_*)	Radius ratio	$0.1146^{+0.0010}_{-0.0011}$	$0.1075^{+0.0018}_{-0.0018}$	$0.108^{+0.0018}_{-0.0019}$
R_p	Planet radius ($R_\oplus$)	$3.66^{+0.12}_{-0.12}$	$3.44^{+0.12}_{-0.12}$	$3.45^{+0.12}_{-0.12}$
R_p	Planet radius ($R_{\rm J}$)	$0.327^{+0.011}_{-0.011}$	$0.306^{+0.011}_{-0.011}$	$0.308^{+0.011}_{-0.011}$
δ_p	Transit depth	$0.01314^{+0.00024}_{-0.00025}$	$0.01155^{+0.00038}_{-0.00039}$	$0.01167^{+0.00040}_{-0.00041}$
a/R_*	Scaled semimajor axis	$24.47^{+0.33}_{-0.33}$	$21.09^{+0.57}_{-0.59}$	$21.29^{+0.55}_{-0.64}$
a	Semimajor axis (from a/R_* and R_*)	$0.0334^{+0.0012}_{-0.0011}$	$0.0287^{+0.0012}_{-0.0012}$	$0.029^{+0.0012}_{-0.0012}$
i	Transit inclination (deg)	$88.068^{+0.046}_{-0.046}$	$87.16^{+0.18}_{-0.21}$	$87.24^{+0.18}_{-0.23}$
b	Impact parameter	$0.8252^{+0.0092}_{-0.0096}$	$0.628^{+0.032}_{-0.037}$	$0.619^{+0.037}_{-0.043}$
e	Eccentricity	$0.0^{+0.0}_{-0.0}$	$0.428^{+0.050}_{-0.049}$	$0.409^{+0.041}_{-0.039}$
ω	Argument of periastron (deg)	$90.0^{+0.0}_{-0.0}$	$120.0^{+12.0}_{-14.0}$	$106.0^{+13.0}_{-16.0}$
$T_{\rm eq}$	Equilibrium temp. (assuming $a = 0$)	$458.3^{+8.8}_{-8.7}$	$494.0^{+11.0}_{-11.0}$	$492.0^{+11.0}_{-11.0}$
$T_{\rm eq}$	Equilibrium temp. (assuming $a = 0.3$)	$320.8^{+6.2}_{-6.1}$	$345.7^{+8.0}_{-7.8}$	$344.3^{+8.0}_{-7.8}$
S	Insolation flux ($S_\oplus$)	$7.35^{+0.58}_{-0.55}$	$9.91^{+0.95}_{-0.86}$	$9.75^{+0.94}_{-0.85}$
T_{14}	Transit duration (days)	$0.03398^{+0.00027}_{-0.00024}$	$0.03182^{+0.00036}_{-0.00037}$	$0.03162^{+0.00037}_{-0.00035}$
T_{23}	Transit duration (days)	$0.01454^{+0.00091}_{-0.00090}$	$0.02212^{+0.00063}_{-0.00065}$	$0.02208^{+0.00068}_{-0.00071}$
τ	Ingress/egress duration (days)	$0.00972^{+0.00042}_{-0.00042}$	$0.00485^{+0.00040}_{-0.00039}$	$0.00477^{+0.00046}_{-0.00042}$
K	RV semiamplitude (m s^{-1})	$24.7^{+7.2}_{-6.8}$	$27.9^{+6.5}_{-6.0}$	$32.2^{+9.7}_{-9.4}$
m_p	Planet mass ($M_\oplus$)	$24.0^{+7.1}_{-6.6}$	$24.5^{+5.7}_{-5.2}$	$28.5^{+8.5}_{-8.3}$
$\sigma_{\rm HPF}$	HPF RV jitter (m s^{-1})	$13.9^{+6.9}_{-5.3}$	$1.8^{+5.1}_{-1.4}$	$42.9^{+7.2}_{-6.5}$
γ	HPF RV offset (m s^{-1})	$-5.0^{+13.0}_{-12.0}$	$4.0^{+16.0}_{-16.0}$	$-4.0^{+7.5}_{-7.5}$
Derived Stellar Parameters				
ρ	Stellar density (g cm^{-3})	$22.83^{+0.92}_{-0.91}$	$14.6^{+1.2}_{-1.2}$	$15.0^{+1.2}_{-1.3}$
GP Hyperparameters for RVs				
$\sigma_{\rm GP}$	GP RV amplitude (m s^{-1})	$34.8^{+8.6}_{-6.6}$	$41.0^{+11.0}_{-7.9}$	...
α	GP inverse timescale (day^{-2})	$13^{+90}_{-10} \times 10^{-6}$	$15^{+70}_{-1} \times 10^{-8}$	...
Γ	GP frequency structure parameter	$8.0^{+1.1}_{-1.1}$	$6.75^{+0.93}_{-1.2}$	...
$P_{\rm GP}$	GP kernel periodicity parameter (days)	$1.88219^{+0.00034}_{-0.00032}$	$1.88203^{+0.00032}_{-0.00031}$	...

Note. We adopt the values for model RV2, as it is statistically favored over the other two models.

6.2. Derived Parameters

Figure 2 shows the K2 transits along with the nine ground-based transits observed and analyzed in this work. The transits on the nights of 2018 December 21 and 2019 January 4 were performed simultaneously with the RM effect observations further discussed in Section 7. The shorter cadence of the ground-based observations compared to the 30 minute cadence K2 observations allows us to resolve the transit shape better, resulting in more precise planet parameters. Table 5 compares the best-fit parameters from the three models considered in this work.

Figure 3 compares the resulting phased RV plots for the three different models considered. The derived best-fit RV semiamplitudes for the three models are $K_{\rm RV1} = 24.7^{+7.2}_{-6.8}$, $K_{\rm RV2} = 27.9^{+6.5}_{-6.0}$, and $K_{\rm RV3} = 32.2^{+9.7}_{-9.4}$ m s^{-1}. This results in mass estimates of $M_{\rm RV1} = 24.0^{+7.1}_{-6.6}$, $M_{\rm RV2} = 24.5^{+5.7}_{-5.2}$, and $M_{\rm RV3} = 28.5^{+8.5}_{-8.3}$ $M_\oplus$ for the three models. We see that all three models result in consistent mass estimates. We note that the GP RV amplitudes for models RV1 and RV2 are similar to $\sigma_{\rm GP,RV1} = 35^{+9}_{-7}$ and $\sigma_{\rm GP,RV2} = 41^{+11}_{-8}$ m s^{-1}. As expected, we see that for model RV3—which does not employ a GP—the white-noise error term significantly increases to compensate for

the additional correlated noise, with $\sigma_{\rm w,RV1} = 13.9^{+6.9}_{-5.3}$, $\sigma_{\rm w,RV2} = 1.8^{+5.1}_{-1.4}$, and $\sigma_{\rm w,RV3} = 42.9^{+7.2}_{-6.5}$ m s^{-1}.

To check which model among models RV1, RV2, and RV3 is statistically favored, we use the log-evidence values calculated by the dynesty dynamic nested sampler. As the estimated errors of the log evidences can be underestimated by nested sampling algorithms (see, e.g., Espinoza et al. 2019; Nelson et al. 2020), to get an accurate estimate of the distribution in the log-evidence values for each model, we run each joint-fit model, RV1, RV2, and RV3, six separate times. In doing so, we obtain log-evidence values of $\ln Z = 25828.7 \pm 9.9$, 25875.4 ± 4.1, and 25869.9 ± 4.2, respectively, where the value reported is the mean of the six runs for each model and the uncertainty estimate is the standard deviation of the six runs. We note that the scatter in the log-evidence values (~10 for model RV1 and ~4 for models RV2 and RV3) is substantially larger than the internal uncertainty estimate of ~0.5 reported from the dynesty sampler for each individual run. Even so, within each group of six runs for models RV1, RV2, and RV3, the resulting output posteriors are fully consistent. Among the three models, we see that the two eccentric models RV2 and RV3 are favored over the circular model RV1.
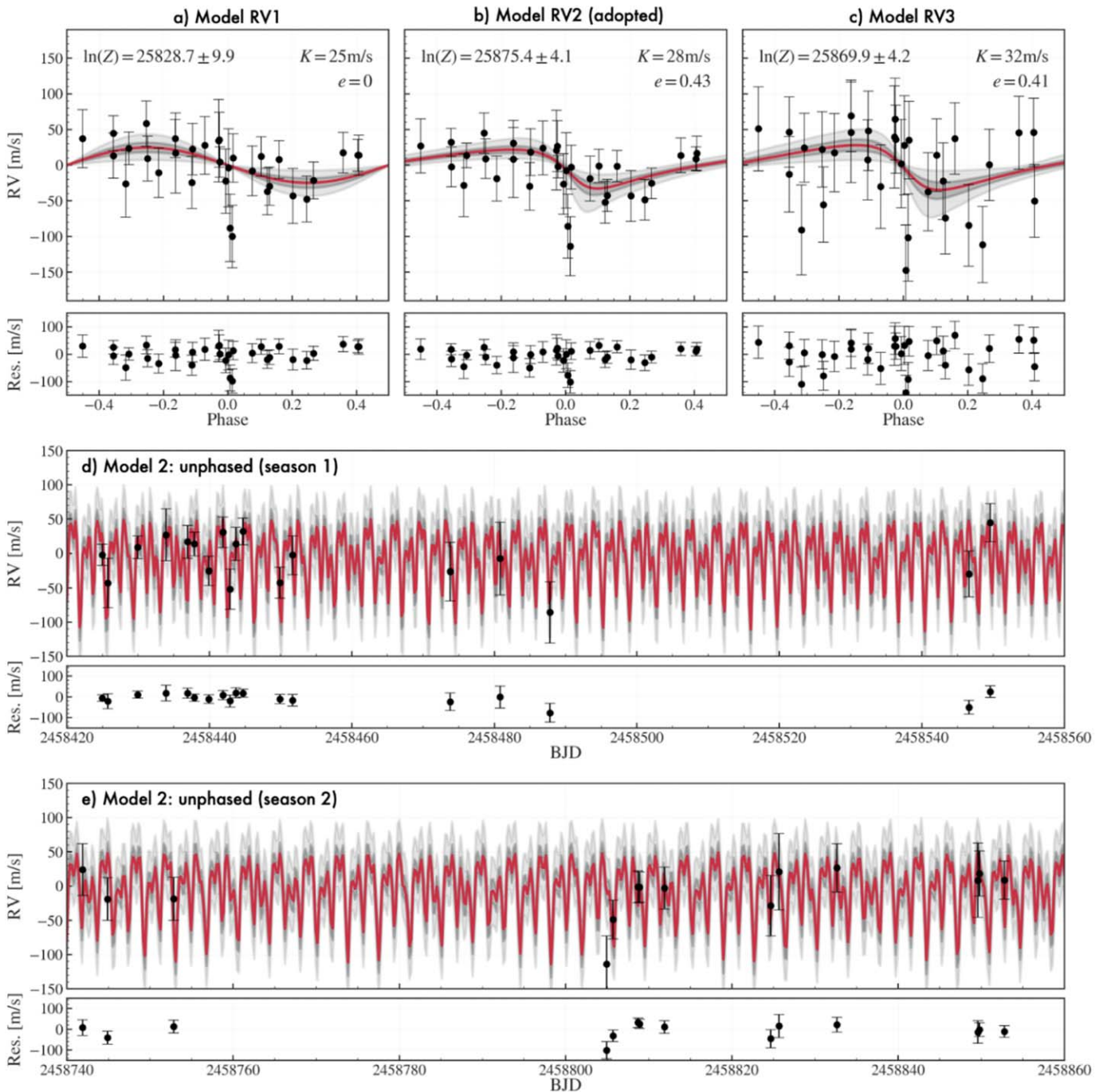
Figure 3. Out-of-transit RVs of K2-25 from HPF comparing the resulting RV models from models (a) RV1, (b) RV2, and (c) RV3 with the associated residuals shown in the corresponding lower panels. The 50th percentile best-fit models are shown in red. The gray shaded regions show the 1σ (darker gray) and 3σ (lighter gray) estimated model confidence bands. The log evidence for the three models is $\ln Z = 25{,}828.7 \pm 9.9$, $25{,}875.4 \pm 4.1$, and $25{,}869.9 \pm 4.2$, respectively, showing a significant preference for the eccentric models (models RV2 and RV3). We adopt model RV2 due to the statistical preference over model RV3, with $\Delta \ln Z \sim 5$ over model RV3. (d) and (e) Nonphased RVs as a function of time for two observing seasons (approximately 1 yr apart). The red curve shows the best-fit GP and Keplerian model. The gray shaded regions show the 1σ (darker gray) and 3σ (lighter gray) estimated model confidence bands.

Between models RV2 and RV3, we see a statistical preference ($\Delta \ln Z \sim 5$) in favor of model RV2. From Table 5, we see that the derived planet parameters, including the semiamplitude, mass, and eccentricity for models RV2 and RV3, are fully consistent. Given the statistical preference, and the fact that we know that K2-25 is a young and active star with a well-characterized stellar rotation period that is explicitly modeled in model RV2, we elect to adopt the values from

model RV2. We compared the distribution of the best-fit residuals of the HPF RVs from model RV2 to a normal distribution using the Kolmogorov–Smirnov test, from which we obtain a p-value of 6.5×10^{-8}. This suggests that the distribution of the RV residuals is indistinguishable from a normal distribution and that our model (one-planet Keplerian along with a quasiperiodic GP) can accurately model the observed RVs.
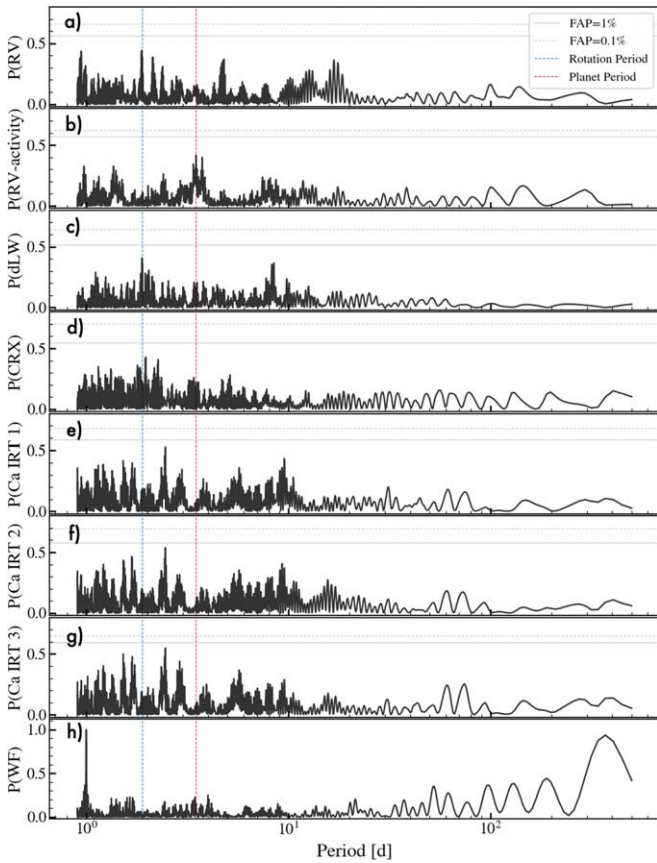
Figure 4. The LS periodograms of the HPF RVs along with different activity indicators. The stellar rotation period ($P = 1.88$ days) and planet period ($P = 3.48$ days) are highlighted with dashed blue and red lines, respectively. False-alarm probabilities of 1% and 0.1% calculated using a bootstrap method are denoted with the gray solid and dashed lines, respectively. (a) HPF out-of-transit RVs used for the mass measurement of K2-25b. (b) Same as panel (a) but after removing the best-fit GP model from model RV2. This shows that the known planet peak becomes more significant. (c) dLW activity indicator, showing a clear peak at the known rotation period. (d) CRX activity indicator. (e)–(g) Ca II IRT indices for the three Ca II IRT lines. (h) WF of the HPF RVs, showing a clear sampling peak at 1 day. The power in panels (a)–(g) is normalized using the formalism in Zechmeister & Kürster (2009), and panel (h) is normalized so that the highest peak is unity.

6.3. Stellar Activity from HPF Spectra

To further study the activity of the star, we measured a number of stellar activity indicators from the HPF spectra. Figure 4 shows the generalized Lomb–Scargle (LS) periodograms of the out-of-transit RVs we used for our mass measurement, along with an array of different activity indicators measured from the HPF spectra, including the differential line width (dLW), chromatic index (CRX), and line indices of the three Ca II infrared triplet (IRT) lines. To calculate the LS periodograms, we used the periodogram functions in the `astropy.timeseries` package, and the false-alarm probabilities[26] were calculated using the `bootstrap` method implemented in this same package. Additionally, in Figure 4, we show the window function (WF) of our RV observations. All of the periodograms in Figure 4 are normalized using the formalism in Zechmeister & Kürster (2009), except the WF is normalized such that the highest peak

---

[26] Although the false-alarm probability is commonly used in periodogram analysis in RV data, it has known limitations (see, e.g., discussion in Fischer et al. 2016).

has a power of 1. Table C1 in Appendix C lists the values of the RVs and the activity indicators used in this work.

To measure these indicators, we follow the definition and procedures in the SERVAL pipeline (Zechmeister et al. 2018). To measure the Ca II IRT indicators, we measure the mean flux in a 30 km s^{-1} wide region centered on the three Ca II IRT line centers, and we use two offset bands (to the right and left of the line center, 100 km s^{-1} wide) as reference regions to measure line indices as defined in Equation (27) in Zechmeister et al. (2018),

$$I = \frac{\langle f_0 \rangle}{0.5(\langle f_1 \rangle + \langle f_2 \rangle)}, \tag{5}$$

where $\langle f_0 \rangle$ is the mean flux around the line center, and $\langle f_1 \rangle$ and $\langle f_2 \rangle$ are the mean fluxes around the reference regions. The exact locations of the line center and offset regions we used are given in Table A1 in Appendix A.

From Figure 4(a), we see a clear peak in the RV periodogram at the known rotation period, indicative of rotationally modulated RV variations, e.g., due to starspots. This interpretation is further strengthened by the fact that we see a clear peak in the periodogram of the dLW indicator at the known rotation period (Figure 4(c)). In Figure 4(b), we show the periodogram of the RVs after subtracting the best-fit GP activity model, demonstrating that after removing the GP model, the peak at the stellar rotation is significantly suppressed, and the peak at the planet period increases in significance. The CRX indicator does not show any clear evidence of periodic variations in the chromaticity of the RVs at either the stellar rotation period or the planet period. Interestingly, in Figures 4(e)–(g), we do not see clear peaks in the Ca II IRT activity indicators at the rotation period; rather, we see a clear peak in all three indices at 2.46 days. We speculate that this could indicate that the active chromospheric regions traced by the Ca II IRT lines could have a different characteristic evolution timescale than the rotation period of the star.

6.4. RV Injection and Recovery Tests

To test that our RV precision and the RV sampling are sufficient to accurately constrain the Keplerian parameters of K2-25b, we performed two series of injection and recovery tests, broadly following the methodology in Klein & Donati (2020). For both series of tests, we injected a signal with known Keplerian parameters (P, T_C, K, ω, e) and GP hyperparameters (P_{GP}, σ_{GP}, α_{GP}, Γ_{GP}), along with a white-noise parameter (σ_w). The values of the parameters for the two tests, along with the priors used for the recovery, are given in Table B1 in Appendix B. We placed informative Gaussian priors on the orbital period (P), transit center (T_C), GP period (P_{GP}), and GP frequency structure parameter (Γ_{GP}), and we placed broad uninformative priors on the other parameters (same priors as used for fit RV2). For the first series of tests (test I), we set the GP amplitude $\sigma_{GP} = 42$ m s^{-1} and other parameters to values similar to the nominal 50th quantile values from our adopted RV2 fit in Table 5 (see exact values injected in Table B1 in Appendix B). For the second series of tests (test II), we increased the injected GP amplitude to its 95th percentile value from our adopted RV2 model in Table 5, corresponding to $\sigma_{GP} = 64.6$ m s^{-1}, to check if the injected Keplerian parameters—in particular, K and e—could be

reliably recovered if the level of the correlated noise is higher. For both tests, we repeated the injection and recovery 200 times, and we then inspected the resulting posteriors calculated using `juliet` from each individual run.

Figure B1 in Appendix B shows the distribution of mean values from test I for a few select parameters of interest: K, ω, e, σ_{GP}, α_{GP}, and σ_w. We see that for all parameters, the distribution of the recovered values is fully consistent with the known injected value. Further, Figure B2 in Appendix B compares the distribution of all 200 posteriors for σ_{GP}, K, and e for both series of injection and recovery tests. To compare the distribution of the synthetic residuals to a normal distribution, we used the Kolmogorov–Smirnov test, from which we see that all data sets have a p-value $< 10^{-5}$ (with most data sets showing a p-value $< 10^{-7}$), suggesting that the best-fit residuals from the synthetic tests are indistinguishable from a normal distribution. Although σ_{GP} shows broad posteriors and is relatively poorly constrained, in both series of tests, the true values of K and e are consistently recovered. For test I, which assumes $\sigma_{GP} = 42$ m s^{-1}, the true value of K is within the 68% and 95% credible intervals in 80% and 99.7% of the cases, respectively. For test II, even with the higher injected value of $\sigma_{GP} = 64.6$ m s^{-1}, the true value of K is reliably recovered within the 68% and 95% credible intervals in 75% and 97% of the cases, respectively. We conclude that the number and sampling of the HPF RVs is sufficient to accurately constrain the Keplerian planet parameters.

7. The RM Effect of K2-25

7.1. RM Model

We model the RM effect using the prescription given in Hirano et al. (2010, 2011). Specifically, we use Equation (26) from Hirano et al. (2011), which gives the RM velocity anomaly as

$$
\Delta v = -\left(\frac{2(\beta + \sigma_{RM})^2}{2\beta^2 + \sigma_{RM}^2} \right)^{3/2} f v_p
$$
$$
\times \left(1 - \frac{v_p^2}{(2\beta^2 + \sigma_{RM}^2)} + \frac{v_p^4}{2(2\beta^2 + \sigma_{RM}^2)^2} \right), \quad (6)
$$

where β indicates the best-fit Gaussian dispersion (in km s^{-1}) of the intrinsic line broadening in the absence of stellar rotation, and σ_{RM} indicates the Gaussian line width component arising from stellar rotation (see Hirano et al. 2010 for details). Here we set β to the width of the HPF resolution element, i.e., $\beta = 5.45 \pm 0.5$ km s^{-1}, where the error bar accounts for any effects of macroturbulence and/or other nonstellar rotation processes that could broaden the line profile. The f parameter denotes the fraction of the star being blocked by the planet during the transit as a function of time (i.e., $f = 1 - F$, where F is the photometric transit model), and v_p denotes the subplanet velocity (in km s^{-1}), i.e., the velocity of the star being blocked by the planet as a function of time during the transit. As discussed in Hirano et al. (2011), σ_{RM} describes the dispersion of a Gaussian approximating the stellar rotational kernel, and here we follow Hirano et al. (2010) and assume $\sigma_{RM} = v \sin i_* / 1.31$. We neglect any differential rotation, as Dmitrienko & Savanov (2017) showed that the differential rotation of K2-25b is small, or

$\Delta\Omega = 0.0071 \pm 0.002$ rad day^{-1}, and thus negligible during the transit.

To model the RM effect, we model all three transits jointly. For the fit, we included the bulk RV motion imposing informative priors on the Keplerian orbital parameters from our best-fit orbital values from model RV2 in Table 5. In addition, we placed an informative Gaussian prior on the $v \sin i_*$ using our $v \sin i_*$ value measured from the HPF spectra. To account for possible systematics between the transits (e.g., due to stellar activity and/or instrumental systematics), we added an independent RV offset parameter γ for each individual transit. We sampled the limb-darkening parameters using the q_1 and q_2 parameterization described in Kipping (2013) and fully sampled them across the whole valid range from zero to 1 to minimize any biases on the RM effect anomaly due to limb-darkening effects. To account for the smoothening of the finite exposure times of our RV observations, we supersampled the model seven times and resampled the model according to the exposure time of $\sim$300 s. We calculated the bulk RV model using the `radvel` Python package (Fulton et al. 2018). To calculate the transit fraction f, we used the `batman` package (Kreidberg 2015), calculating the transit flux and setting $f = 1 - F$, where F is the transit model from `batman`. Before we started the Markov Chain Monte Carlo (MCMC) sampling, we found the global most probable solution using the `PyDE` differential evolution optimizer (Parviainen 2016). We then initialized 100 MCMC walkers in the vicinity of the global most probable solution using the `emcee` affine-invariant MCMC sampling package (Foreman-Mackey et al. 2013). We ran the 100 walkers for 25,000 steps, and after removing the first 2000 steps as burn-in and thinning the chains by a factor of 100, the Gelman–Rubin statistic of the resulting chains was within $<$1% of unity, which we consider well mixed.

To test the impact of our assumptions about stellar activity on λ, we performed four additional fits:

1. a joint fit with a single RV offset parameter γ,
2. a joint fit with a single RV offset parameter γ after subtracting our best-fit GP activity model (from model RV2 in Table 5) from the RVs,
3. a joint fit with three independent RV offset parameters γ and removing the prior on the semiamplitude, and
4. a joint fit with three independent RV offset parameters γ and removing the prior on $v \sin i_*$.

All fits resulted in fully consistent constraints on λ suggesting a well-aligned system, although we note that the fit with a single RV offset parameter resulted in a slightly higher uncertainty estimate on λ, or a constraint of $\lambda = 0° \pm 24°$. From the GP activity model constrained from our out-of-transit RVs, we note that the expected RV variation during the three transits observed is slowly varying and significantly smaller ($<$5 m s^{-1}) than the observed RM amplitude of $\sim$65 m s^{-1} and thus is effectively modeled out with independent offsets between the transits. In comparing the Bayesian information criterion (BIC) and Akaike information criterion (AIC; Akaike 1974), the models show a statistical preference (ΔAIC $\sim$ 9) for models that allowed for independent offsets between the transits. We note that using the BIC and AIC in this case is heuristic, as more data points would be formally needed for these criteria to be in the asymptotic regime where they are accurate and justified for model

Table 6
Median Values and Associated 16th and 84th Percentile Values from Our
RM Fit

Parameter	Description	Value
Model Likelihood Parameters		
χ^2_ν	Reduced χ^2	1.04
DOF	Degrees of freedom	25
MCMC Parameters		
λ	Sky-projected obliquity (deg)	3 ± 16
$v \sin i_*$	Rotational velocity (km s^{-1})	8.9 ± 0.6
γ_1	RV offset (m s^{-1})	-10^{+28}_{-28}
γ_2	RV offset (m s^{-1})	58^{+27}_{-26}
γ_3	RV offset (m s^{-1})	-95^{+29}_{-28}
q_1	Linear limb-darkening parameter	$0.47^{+0.35}_{-0.33}$
q_2	Quadratic limb-darkening parameter	$0.44^{+0.36}_{-0.31}$
β	Intrinsic stellar line width	$5.41^{+0.49}_{-0.50}$
Derived Parameters		
ψ	3D obliquity (deg)	17^{+11}_{-8}

comparison. To allow for flexibility to take out potential systematic offsets between the three transits, we report the resulting posterior constraint from the fit assuming three independent RV offset γ parameters in Table 6. We further note that the fit where we allowed $v \sin i_*$ to vary freely resulted in a fully consistent λ value and yielded $v \sin i_* = 11.6 \pm 3$ km s^{-1}, which is consistent with the measured $v \sin i_* = 8.8 \pm 0.6$ km s^{-1} from the HPF spectra at the 1σ level.

7.2. Results

Figure 5 shows the three RM effect observations using HPF, along with our best-fit RM model (RM amplitude $\sim$65 m s^{-1}) and 1σ, 2σ, and 3σ shaded regions. Table 6 summarizes the resulting best-fit posterior values, showing that we obtain a sky-projected obliquity constraint of $\lambda = 3° \pm 16°$. To further visualize and compare the observed RVs to the best-fit RM model, in Figure 6, we show all three of the transits in Figure 5 phased to the transit ephemeris and binned to a 5 minute cadence using a weighted average. The resulting median RV error is 55 m s^{-1} in the 5 minute bins. The RM model is shown with the bulk RV model and RV offset parameters removed for clarity.

In addition to the sky-projected obliquity listed in Table 6, we calculate the true obliquity angle ψ using the equation

$$\cos \psi = \sin i_* \cos \lambda \sin i + \cos i_* \cos i, \qquad (7)$$

where i_* is the stellar inclination, i is the transit inclination, and λ is the sky-projected obliquity angle. Using Equation (7) above and our $\lambda = 3° \pm 16°$ constraint from Table 6, $i = 87°.13 \pm 0°.17$ from Table 5 (model RV2), and $i_* = 90° \pm 12°$ constraint from Table 2, we obtain the following constraint on $\psi = 17^{+11}_{-8}°$. Integrating the resulting posterior, we can say that $\psi < 30°$ with 89% confidence, which is compatible with a well-aligned system.

8. Discussion

With its known age and characterized 3D orbital architecture, K2-25b is an interesting laboratory to test different formation scenarios. In Section 8.1, we compare our improved ephemerides to the ephemerides of other recent literature on

this system. In Section 8.2, we discuss the composition of K2-25b, showing that at its observed mass and radius, it is consistent with a water-rich world, or a rocky core with a small H/He envelope. In Section 8.3, using our mass constraint, we discuss the possibility for atmospheric characterization through transmission spectroscopy with JWST in the future. In Section 8.4, we discuss our obliquity constraint, which is suggestive of a well-aligned orbit, and place it in context with other measurements in the literature. Finally, our detailed characterization of the different orbital parameters of the planet allows us to place informative constraints on different formation scenarios, which we discuss in Section 8.6.1.

8.1. Improved Ephemeris

Figure 7 shows the improved ephemeris derived by jointly modeling the K2 and ground-based transits (model RV2 in Table 5). In blue, we show our ephemeris derived from the K2 data only ($T_{0,K2} = 2,457,062.5790 \pm 0.0005$ and $P_{K2} = 3.484547 \pm 0.000040$), which agrees well with the ephemeris derived in Mann et al. (2016a), also from the K2 data. Our K2-only ephemeris results in a transit timing uncertainty of $\sim$35–40 minutes at the start of the JWST era, nominally in 2021. Further, we see that our joint-fit ephemeris (shown in black in Figure 7) is fully consistent within the 1σ error bars of our K2-only ephemeris. Our joint-fit ephemeris results in a factor of $\sim$150 improvement in the transit timing precision from the K2 data only, yielding a timing uncertainty of $\sim$20 s at the start of the JWST era, nominally in 2021, which will be important for scheduling follow-up observations in the future. Additionally, Figure 7 shows that our joint fit is in excellent agreement with the transit ephemeris presented in Thao et al. (2020) derived from photometry from K2, Spitzer, and ground-based observations.

8.2. Composition

To compare the possible composition of K2-25b to other planets, in Figure 8, we plot K2-25b along with other planets in the exoplanet mass–radius plane.[27] In Figure 8, we only show planets with fractional errors on mass and radius that are better than 25%, as otherwise, their mass and radius values are consistent with a wide array of planet composition models. The gray shaded region indicates planets with iron content exceeding the maximum value predicted from models of collisional stripping (Marcus et al. 2010). The solid lines are theoretical mass–radius curves assuming a constant density from Zeng et al. (2019). From Figure 8, we see that at a radius of $R = 3.44\ R_\oplus$, K2-25b is similar in size to two other well-studied M dwarf planets, GJ 436b ($4.2\ R_\oplus$; Maciejewski et al. 2014) and GJ 3470b ($4.57\ R_\oplus$; Awiphan et al. 2016), which are highlighted in Figure 8. With a mass of $M = 24^{+5.7}_{-5.2}\ M_\oplus$, K2-25b is similar in mass to GJ 436b ($M = 22.1\ M_\oplus$; Maciejewski et al. 2014) but more massive than GJ 3470b ($M = 13.9\ M_\oplus$; Awiphan et al. 2016). Interestingly, both GJ 436b and GJ 3470b are known to be experiencing substantial atmospheric outflows resulting in significant atmospheric mass loss throughout their lifetimes (see, e.g., Ehrenreich et al. 2015; Bourrier et al. 2018a and Ninan et al. 2019, respectively). The possibility that K2-25b is experiencing outflows is further discussed in Section 8.3.

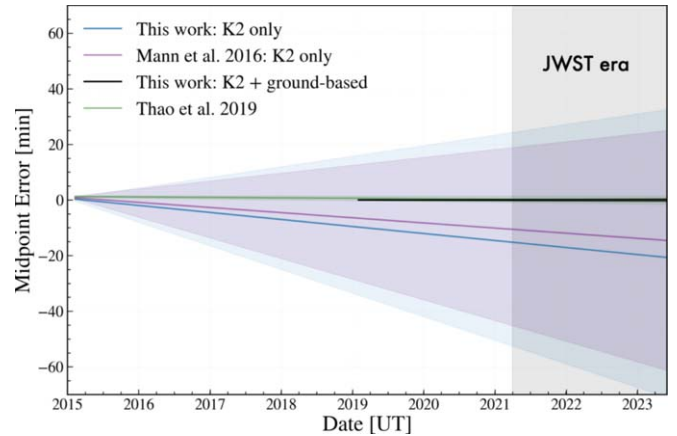[27] Data retrieved from the NASA Exoplanet Archive (Akeson et al. 2013) in 2019 November.
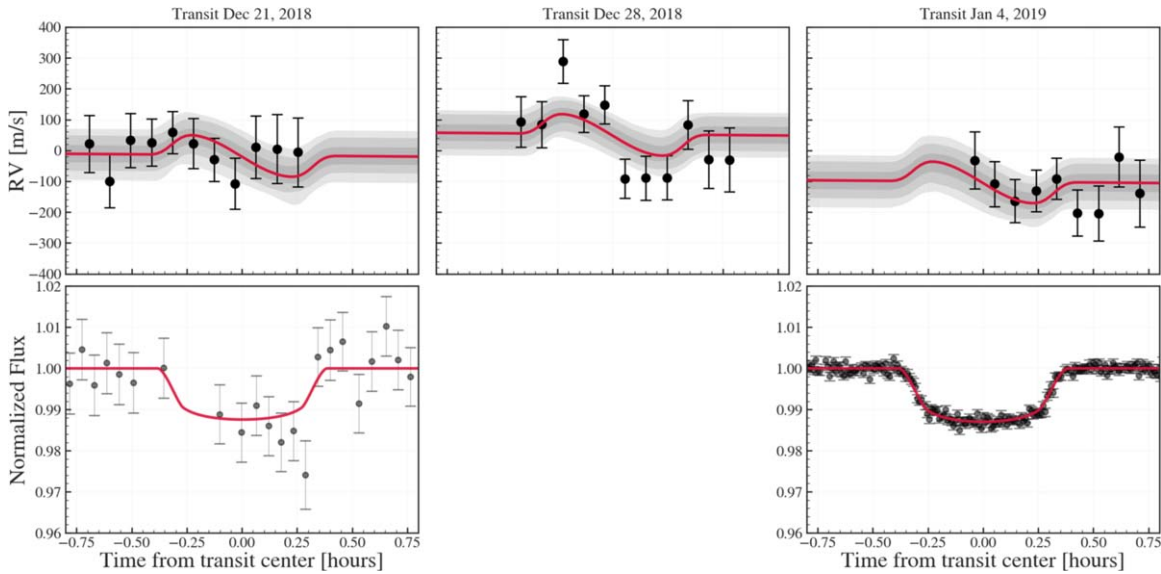
Figure 5. Upper panels: three RM effect transits as observed with HPF (black points), along with the best-fit joint RM effect model shown in red. The RM model includes the bulk RV shift, and an independent RV offset parameter γ is included for each transit to account for stellar activity and/or instrumental effects. The gray shaded regions show the 1σ, 2σ, and 3σ confidence regions. Lower panels: two simultaneous photometric transits from HDI (2018 December 21) and ARCTIC (2019 January 4) shown in black, along with the best-fit transit model (model RV2 in Tables 4 and 5). The HDI observations were performed without a diffuser due to the Moon contamination that night. No starspot crossing events are seen in the simultaneous transit observations, which otherwise would complicate the RM effect analysis. Figure 6 shows the three RM effect observations phased together and binned to 5 minute bins for further visual inspection.
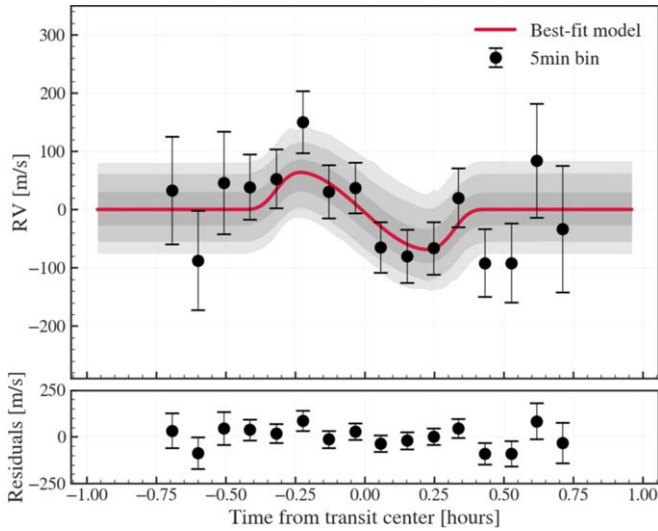
Figure 6. The RM effect of K2-25b after combining the three jointly fitted RM effect observations shown in the upper panels in Figure 5. The best-fit RM model (red curve) has the bulk RV motion and RV offset parameters removed. The black points show the data binned to a 5 minute cadence. The gray shaded regions show the 1σ, 2σ, and 3σ confidence bands.

Figure 7. Updated transit ephemeris for K2-25b into the JWST era. Our ephemeris derived from the K2 photometry only (blue shaded region) agrees well with the ephemeris provided in Mann et al. (2016a; purple). Our improved ephemeris (model RV2 in Table 5) results in an error of $\sim$20 s at the beginning of the JWST era, nominally in 2021, and is in excellent agreement with the ephemeris provided in Thao et al. (2020) derived from data from K2, Spitzer, and additional ground-based observations. The shaded regions show the 1σ error estimates.

There are degeneracies in the composition of planets with radii between 2 and 4 $R_\oplus$: these planets could either have rocky cores with H/He envelopes or be water-rich worlds that contain a significant amount of multicomponent water dominated ices/fluids in addition to rock and gas (Zeng et al. 2019). As such, from knowing the masses and radii of a planet alone, we cannot discern between the different solutions (Adams et al. 2008).

Given this known degeneracy, to explore the range of possible compositions for K2-25b, we overplot a number of different compositional growth models in the exoplanet mass–radius plane from Zeng et al. (2019). To place a quantitative estimate on the possible H/He fraction of K2-25b, we modeled the composition of K2-25b assuming a two-layer thermal model consisting of a rocky core and an H/He atmosphere using the models presented in Lopez & Fortney (2014). In this model, the H/He envelope is the dominant driver of the size of the planet. Assuming this two-component model, we linearly interpolated the tables presented in Lopez & Fortney (2014), and, together with the posteriors in the observed mass and radius of K2-25b, we estimated that K2-25b has an envelope mass fraction of $5.3^{+1.2}_{-0.9}\%$. The 50th percentile model that best fits the observed mass and radius constraints of K2-25b is shown by the red curve in Figure 8, with the 1σ error intervals denoted by the red shaded region.

Despite these degeneracies, with more mass measurements of planets in young clusters (see, e.g., Barragán et al. 2019), we
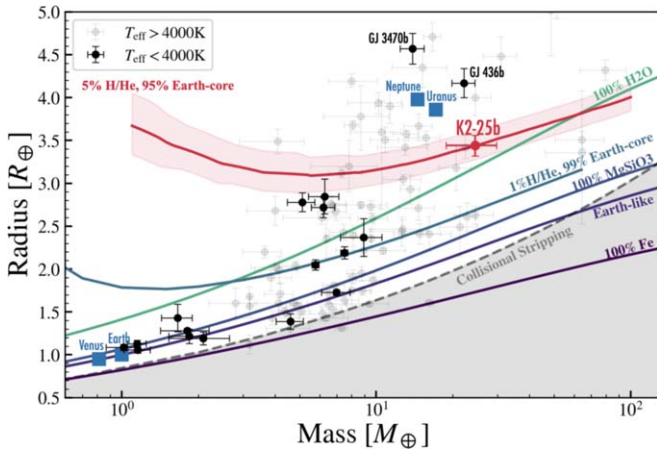
Figure 8. Planet K2-25b compared to other similar-sized planets in the exoplanet mass–radius plane for M dwarf planets. The M dwarf planets ($T_{eff} < 4000$ K) are denoted with black circles, and planets orbiting hotter stars are shown with faint gray circles. Blue squares show solar system planets. The red curve shows our best-fit model from interpolating the two-layer composition model of Lopez & Fortney (2014), assuming a rocky core capped by an H/He envelope, resulting in an H/He mass fraction of 5%. The red shaded region shows the associated 68% credible interval. The other solid lines show the composition models of Zeng et al. (2019). The gray shaded region indicates planets with iron content exceeding the maximum value predicted from models of collisional stripping (Marcus et al. 2010). Planet K2-25b is similar in size to the well-studied M dwarf planets GJ 436b and GJ 3470b.

can start to gain further insights into the exoplanet mass–radius distribution as a function of age, which can help place further constraints on planet formation mechanisms and how time-dependent processes such as photoevaporation sculpt the exoplanet mass–radius plane.

### 8.3. Prospects for Transmission Spectroscopy

With its large transit depth and brightness at NIR wavelengths ($J = 11.3$), K2-25b has been mentioned as a prime candidate for transmission spectroscopy (e.g., Mann et al. 2016a; Thao et al. 2020). Thao et al. (2020) measured and studied the transit depths of K2-25b in different broadband filters via precision ground-based photometry and space-based photometry from Kepler and Spitzer. In Figure 9, we plot the transit depth measurements from Thao et al. (2020) along with our transit depth measurements in the SDSS i' and z' bands. As our transit depth measurement presented in Table 5 assumed a single transit depth for all bands, to measure these transit depths, we conducted two separate transit fits using the `Juliet` program: first, we jointly modeled our five SDSS z'-band transits, and second, we jointly modeled our four SDSS i'-band transits. From Figure 9, we see that our transit depths in these bands agree well with the optical transit depth measurements in Thao et al. (2020). However, as seen in Figure 9, the infrared Spitzer transits from Thao et al. (2020) are statistically smaller than the optical transits. As detailed in Thao et al. (2020), this could potentially be due to starspots causing the transit depths to be less deep. However, like they argued, the impact of starspots on the transit depth in the NIR is likely lower than in the optical. Further, no clear starspot crossing events are observed in their data, the data studied in Kain et al. (2020; although Kain et al. 2020 mentioned a few candidate starspot crossing events), or the transits presented here. As concluded by Thao et al. (2020), while spots can have an impact on the overall transmission spectrum, it is unlikely

that starspots alone could cause the difference in the NIR transit depths. One possible explanation, as mentioned in Thao et al. (2020), is that K2-25b has a predominantly cloudy or hazy atmosphere, causing a flat transmission curve as a function of wavelength.

Thao et al. (2020) used the parametric mass–radius relation from Wolfgang et al. (2016) to estimate a most likely mass for K2-25b of $M = 13$ $M_{\oplus}$ and consider different transmission models assuming planet surface gravities of 6, 9, and 12 m s^{-2}, corresponding to planet masses of 8, 11.5, and 15 $M_{\oplus}$, respectively. All of these mass estimates are lower than our measured mass of $M = 24.5^{+5.7}_{-5.2} M_{\oplus}$, which corresponds to a surface gravity of $g = 20.3 \pm 4.7$ m s^{-2}. As an independent test, we also predicted a mass of $M = 11.5^{+9.1}_{-4.8} M_{\oplus}$ using the mass–radius relation in the `Forecaster` package from Chen & Kipping (2017). In Figure 9, we compare the expected transmission spectrum as calculated with the `pandexo` package (Batalha et al. 2017) for both the predicted mass of 11.5 $M_{\oplus}$ and our measured mass of 25 $M_{\oplus}$. As expected, we see that the transmission features of K2-25b are muted in the more massive case, as the increased mass increases the surface gravity of the planet. This can also be seen if we calculate the transmission spectroscopy metric (TSM) defined in Kempton et al. (2018): using the predicted mass of 11.5 $M_{\oplus}$, we obtain a TSM = 143, while if we use our mass estimate, we estimate a lower TSM = 66^{+21}_{-14}. Our larger mass measurement that mutes the expected transmission features of K2-25b could further help explain—at least partially—the flat transmission features observed by Thao et al. (2020).

Despite our larger mass estimate causing the expected transmission features to be muted, the cloud-rich or hazy atmosphere scenario suggested in Thao et al. (2020) is still a likely possibility. In fact, this would conform with the rising statistical trend that colder planets preferentially show muted and/or flat features in their transmission spectra (Crossfield & Kreidberg 2017). However, to confidently quantify the exact amplitude of the transmission features—which strongly depend on the mass of the planet, which is now known—we argue that additional observations with JWST will be valuable to further confidently rule out or confirm a flat transmission spectrum (particularly the information-rich 1–2 μm region). As an example, in Figure 9, we overplot the expected S/N of JWST/NIRISS in single-object slitless spectroscopy mode using the `gr700xd` grism after five transit observations binned to a resolving power of $R = 50$, showing that even for our large mass of 24.5 $M_{\oplus}$, JWST/NIRISS should have the sensitivity to confidently discern between a clear or cloudy atmosphere. Gaining further insights into K2-25b's atmosphere will be particularly valuable, as this will allow us to put constraints on the atmospheric constituents of this relatively young planet, giving key insights into the atmospheric composition of adolescent planets and planetary atmospheres as a function of time. We note that Wang & Dai (2019) suggested that young, low-density "super-puff" planets—planets with mean density $\rho < 10^{-1}$ g cm^{-3}—could be susceptible to extreme hydrodynamic mass loss that can carry large numbers of small dust particles to high altitudes, which, in turn, can create featureless transmission spectra. However, with K2-25b having a bulk density of $\rho = 3.3 \pm 0.8$ g cm^{-3}, which is substantially larger than the cutoff for "super-puff" planets, this scenario is unlikely to be the case.
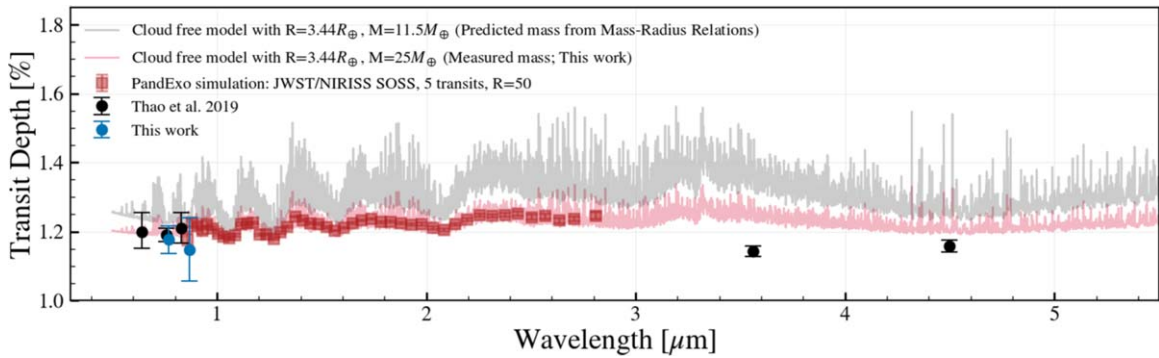
Figure 9. Comparison of transit depth as a function of wavelength for K2-25b from Thao et al. (2020; black points) and this work (blue points) in the SDSS i' and z' bands. We further overlay two expected cloud-free transmission spectra as calculated with the `pandexo` tool for our measured mass of 25 $M_\oplus$ and compare that with the case using the predicted mass of 11.5 $M_\oplus$ estimated using the mass–radius relation in the `Forecaster` package. As expected, our higher mass increases the surface gravity of the planet, which further mutes the expected transmission spectroscopic features.
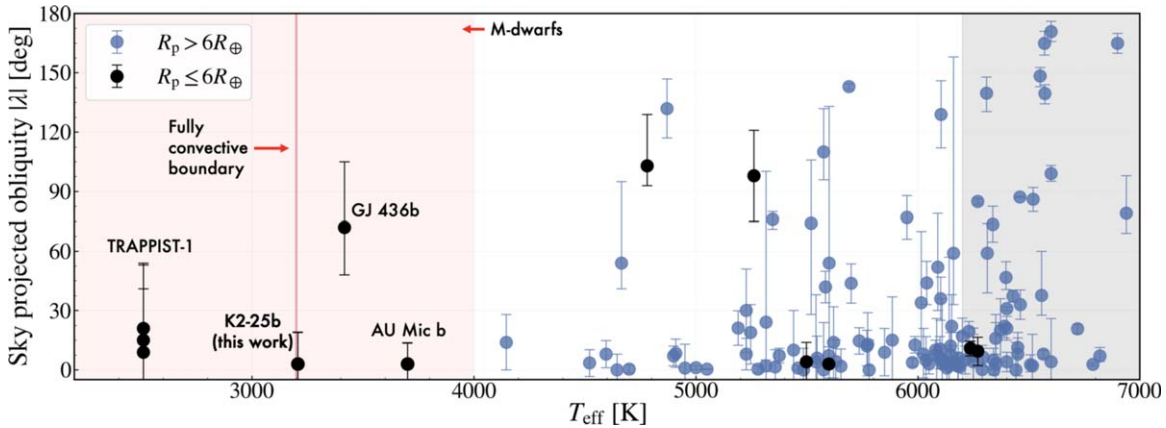
Figure 10. Currently available sky-projected obliquity constraints λ obtained from the TEPCAT database (Southworth 2011) as a function of stellar effective temperature. Small planets ($R < 6\,R_\oplus$) are shown in black, and larger planets are shown in blue. The gray area shows stellar hosts past the Kraft break (Kraft 1967), where stars lose their outer convective layers and become fully radiative. The red shaded region shows M dwarf systems, with the onset of fully convective stars shown by the red solid line. Currently, only four M dwarf planetary systems have their obliquity measured via the RM effect: GJ 436b (Bourrier et al. 2018b), TRAPPIST-1 (Hirano et al. 2018), AU Mic b (Addison et al. 2020; Hirano et al. 2020b; Palle et al. 2020), and K2-25b (this work).

8.4. Obliquity and Orbital Alignment

Figure 10 compares the sky-projected obliquity of K2-25b to currently available sky-projected obliquity measurements of other planetary systems from the TEPCAT[28] database (Southworth 2011); M dwarfs are shaded in red, and the onset of fully convective stars is highlighted by the red solid line. Our obliquity constraint of K2-25b marks the fourth obliquity constraint of an M dwarf planet system via the RM effect, the others being GJ 436b as measured by Bourrier et al. (2018b); AU Mic b as measured by Addison et al. (2020), Hirano et al. (2020a), and Palle et al. (2020); and TRAPPIST-1 as measured by Hirano et al. (2020a). At an age of 600–800 Myr, K2-25b has an intermediate age among these systems; TRAPPIST-1 has an estimated age of 7.6 ± 2.2 Gyr (Burgasser & Mamajek 2017), GJ 436 has an age between 4 and 8 Gyr (Bourrier et al. 2018b), and AU Mic is the youngest with an age of 22 Myr. Interestingly, both K2-25b and GJ 436b have eccentric orbits ($e = 0.43 \pm 0.05$ and 0.1616 ± 0.004, respectively) and are similar in size, but they show different orbital architectures: GJ 436b is observed to have a misaligned orbit, while K2-25b is observed to have an aligned orbit. This could be suggestive of a different formation and subsequent dynamical history. Bourrier et al. (2018b) suggested that von Zeipel–Lidov–Kozai

migration induced by a candidate perturber could explain both GJ 436b's eccentricity and misaligned orbit. However, as we do not see that K2-25b is heavily misaligned, this disfavors von Zeipel–Lidov–Kozai cycles acting on the planet. We further discuss potential formation pathways for K2-25b in Section 8.6.

With only a few obliquity measurements of M dwarf planetary systems published via the RM effect, the orbital architectures of individual M dwarf planetary systems remain relatively unexplored. However, we note that statistical studies suggest that planets orbiting cooler planet hosts have orbits that are, on average, better aligned to their stellar equators than planets orbiting hotter stars. In comparing the rotation distribution of Kepler objects of interest (KOIs) hosting transiting planet candidates to a control sample of single stars without transiting planet candidates, Mazeh et al. (2015) showed that hotter stars ($T_{\rm eff} > 6000$ K) show, on average, lower-amplitude photometric modulations suggesting a broad distribution of obliquities, while cooler KOIs (3500 K $< T_{\rm eff} < 6000$ K) showed, on average, higher-amplitude modulations suggesting well-aligned systems. This result is in broad alignment with the findings of Winn et al. (2010a), Schlaufman (2010), and Albrecht et al. (2012) that hotter stars ($T_{\rm eff} > 6250$ K) hosting close-in gas giants show a broad distribution of obliquities and misalignments, while cooler stars

---

[28] TEPCAT database: https://astro.keele.ac.uk/jkt/tepcat/obliquity.html.

$(T_{eff} < 6250\ \mathrm{K})$ tend to host well-aligned systems. We note that neither of these studies encompassed mid-to-late M dwarfs. In general, across the M dwarf spectral type—and especially for mid-to-late M dwarfs—the occurrence of gas giants is lower than seen around FGK stars (Johnson et al. 2010; Dressing & Charbonneau 2015; Hardegree-Ullman et al. 2019). By further studying the orbital architectures of M dwarf systems, which have a lower occurrence of massive planets, we can gain further insight into the role massive planets play in sculpting the orbital architectures across different exoplanet host stars. The advent of precise NIR spectrographs, such as HPF (Mahadevan et al. 2012, 2014), the Infrared Doppler Instrument (IRD; Kotani et al. 2018), CARMENES (Quirrenbach et al. 2018), SPIROU (Artigau et al. 2014), NIRPS (Wildi et al. 2017), and GIANO-B (Claudi et al. 2018), and red–optical spectrographs on large telescopes, such as MAROON-X (Seifahrt et al. 2016), ESPRESSO (González Hernández et al. 2018), and KPF (Gibson et al. 2016), is opening the doors to the ensemble study of the obliquities of M dwarfs.

8.5. Search for Additional Nontransiting Planets in the HPF RVs

To place an upper limit on a potentially nontransiting second planet in the system, we performed an additional two-planet RV fit of the HPF RVs using `juliet`. As there are no obvious signs of another transiting planet in the system in the K2 data, we only considered the HPF RVs for this fit. We assumed a two-planet model along with a quasiperiodic GP to account for correlated noise due to stellar activity at the known rotation period of the star. We placed Gaussian priors on the orbital parameters of K2-25b derived from the joint fit of the RVs and photometry and used the same priors we placed on the GP hyperparameters as listed in Table 4 for fits RV1 and RV2. For the hypothetical planet c, we placed broad priors on the period (Jeffreys prior from 0.5 to 50 days), time of conjunction (modeled as a transit midpoint uniform from 50 days before the first RV point to 50 days after the last RV point), eccentricity (uniform from zero to 0.95), argument of periastron (uniform prior from $0°$ to $360°$), and RV semiamplitude (uniform from zero to 500 m s^{-1}). To check for evidence of a long-term slope, we also added an RV slope with broad uniform priors.

Figure 11 shows the constraint on the orbital period and mass ($m\sin i$) of the hypothetical planet c. From this, we see that no obvious preferred solution is found. From the posteriors, we place an upper limit on the mass of a possible secondary planet of $m\sin i < 82\ M_\oplus$ at 99.7% confidence (3σ) for periods between 0.5 and 50 days. The red curve in Figure 11 shows a running 99.7% upper limit on the mass as a function of period for smaller period bins. We further note that our constraint on an additional RV slope is consistent with zero slope within the 1σ uncertainties. We additionally compared the log-evidence values we obtained from our `juliet` fit for the two-planet model (two planets, a GP to account for stellar activity, and an RV slope) to a null model assuming only K2-25b in the system (one planet and a GP to account for stellar activity). In doing so, the two-planet model had a log-evidence value of $\ln(Z) = -183.7 \pm 0.5$, while the null one-planet model had a log-evidence value of $\ln(Z) = -170.6 \pm 0.1$, where we have reported the mean and standard deviation of six independent runs of each model to get an accurate estimate of the spread in log-evidence values. We see that the one-planet model is statistically favored with a higher evidence of $\Delta \ln(Z) = 13.1$.
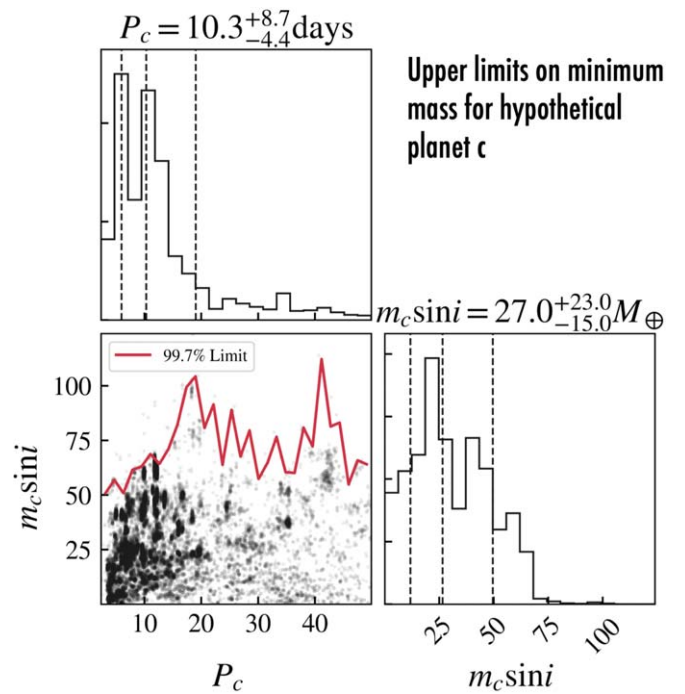
Figure 11. Posterior constraints on a hypothetical nontransiting planet c in the HPF RVs in mass ($m_c \sin i$) and orbital period (P_c) space. We see no obvious evidence for another massive planet in the HPF RVs given the broad posterior constraints. The red curve shows a running 99.7% upper limit (3σ) on the mass as a function of period. Across the full period range considered, we use the posteriors to place an upper mass limit of 82 $M_\oplus$ at 99.7% confidence for periods between 0.5 and 50 days.

With the current RV data in hand, we rule out massive companions with masses $M > 82\ M_\oplus$ at 99.7% confidence with periods between 0.5 and 50 days and conclude that we do not have sufficient evidence to claim another small short-period planet in the system.

8.6. Formation and Subsequent Evolution

Our detailed constraints of K2-25b's planetary properties, including constraints on its mass, eccentricity, volatile content, and obliquity of the host star, allow us to put informative constraints on potential formation scenarios, which we discuss below.

8.6.1. Potential Formation Scenarios

In the core-accretion model of planet formation, planetesimals collide to form protoplanetary cores, which then attract a gaseous envelope (e.g., Bodenheimer & Pollack 1986; Pollack et al. 1996). If the planet core becomes sufficiently massive—after reaching a critical mass M_{crit}—before the gaseous protoplanetary disk dissipates, the protoplanetary core can enter a phase of runaway gas accretion where the planet attracts a massive gaseous envelope. Although the critical core mass is typically quoted as 10 $M_\oplus$, it can vary by orders of magnitude depending on the disk conditions and planetesimal accretion rate (see, e.g., Rafikov 2006). The gaseous envelope is accreted onto the planetary core from the gaseous component of the protoplanetary disk, which only remains present for a few million yr around young stars (Williams & Cieza 2011; Ribas et al. 2015), suggesting that core formation must happen within this time frame. However, traditional core-accretion models

suffer from predicting formation timescales for gaseous planets that are much larger than the disk dissipation timescale (Dodson-Robinson et al. 2009; Rafikov 2011).

In the pebble-accretion model of planet formation, small millimeter-to-centimeter-sized pebbles accrete onto a planetary core (Lambrechts & Johansen 2012; Lambrechts et al. 2014; Lambrechts & Lega 2017). These pebbles are marginally coupled to the nebular gas on orbital timescales, creating sufficient gas drag to enable efficient core formation within the disk dissipation timescale even at large orbital separations (Lambrechts & Johansen 2012). The pebble-accretion model predicts that pebble accretion terminates when the planet reaches the "pebble isolation mass," M_{iso}, the mass when the gravity of the core is strong enough to open a gap in the disk that hinders further accretion of pebbles (Lambrechts et al. 2014). If the pebble isolation mass is greater than the critical core mass and the critical core mass is reached before the disk dissipates of gas, the massive core can rapidly accrete gas to form a gas giant. However, if the pebble isolation mass is not reached, it is reached after most of the disk has dissipated, and/ or it is below the critical core mass, the planet core consists primarily of accreted icy pebbles with a minimal H/He atmosphere. Although the exact value of the pebble isolation mass depends strongly on a number of uncertain disk properties, including aspect ratio, viscosity, local disk structure, and pebble size, the pebble isolation mass for solar-type stars at 5 au has been estimated to be 10–20 $M_{\oplus}$ (Lambrechts et al. 2014), although larger values are also possible depending on the assumed disk properties (see, e.g., Bitsch et al. 2018). The pebble isolation mass increases with the orbital semimajor axis proportional to $a^{3/4}$ (Lambrechts et al. 2014), where a is the semimajor axis of the planetary core. This suggests that planets with massive dense cores cannot form too close to the host star, where the pebble isolation mass is smaller. Further, the pebble isolation mass is expected to decrease for less massive later-type stars according to the following formula from Liu et al. (2019),

$$M_{iso} = 25\left(\frac{M_*}{1M_{\odot}}\right)^{4/3} M_{\oplus}, \qquad (8)$$

where M_* is the mass of the host star, and it is assumed that the planet reaches the isolation mass at the ice-line distance. Assuming K2-25b formed at the ice line and subsequently migrated further in, we calculate an expected isolation mass of ∼5 $M_{\oplus}$.

At its currently observed mass of 24.5 $M_{\oplus}$ with a thin 5% H/He envelope, K2-25b is nominally at odds with the predictions of the core- and pebble-accretion models if it reached its final mass during the full gas disk stage beyond the ice line under certain disk conditions and assumed planetesimal accretion rates. From the core-accretion model, at its currently observed mass, we would have predicted K2-25b to have experienced runaway gas accretion and formed a gas giant, while we instead infer only a thin H/He envelope of ∼5%. From the viewpoint of the pebble-accretion model, we would expect that K2-25b would have reached a nominal maximum core mass that is closer to the isolation mass of ∼5 $M_{\oplus}$ that we estimated from Equation (8) if it formed beyond the ice line. We again acknowledge that the exact value of the pebble isolation mass is uncertain, as it depends strongly on a number of gas disk properties for K2-25b that are not well known.

To arrive at the presently observed mass and explain K2-25b's low inferred H/He content and moderate eccentricity, a possible scenario is that K2-25b grew its mass through the merging of planetary cores. The merging of icy cores has been postulated to explain the observed bimodality in the mass distribution of Neptunes between 2 and 4 $R_{\oplus}$ (Zeng et al. 2019). Although collisional growth could happen at K2-25b's current orbital location after, e.g., in situ formation or disk-driven migration, the planet's current high eccentricity could be more easily excited at larger orbital distances (we discuss its high eccentricity and migration pathways further below). If the seed cores were composed primarily of water ices, Marcus et al. (2010) showed that the collisions of two icy cores tended to stick, yielding a final core of doubled mass. During collisions, it is possible that substantial fractions of H/He envelopes get stripped away (see, e.g., Inamdar & Schlichting 2015, applicable for masses lower than Neptune), which could mean that its atmospheric fraction was somewhat higher in the past (though still not a gas giant).

Lastly, a possible scenario is that K2-25b formed in situ close to its current observed orbit close to the host star (e.g., Batygin et al. 2016), followed by dynamical interactions to explain its current eccentricity. In situ formation has been shown to be able to describe the observed compositional and orbital diversity of super-Earths and mini-Neptunes through inherent variations in the initial formation conditions in the disk (MacDonald et al. 2020). To avoid runaway accretion in an in situ formation scenario, as Lee et al. (2014), MacDonald et al. (2020), and others have argued, the accretion could happen at a later stage, when the disk is partially depleted, then grow through giant impacts and accrete a gaseous envelope in a depleted nebula. However, a challenge for this formation scenario is that in situ formation generally predicts eccentricities that are lower than K2-25b's currently observed eccentricity (see, e.g., MacDonald et al. 2020).

8.6.2. Potential Migration Histories and Eccentricity

From the viewpoint of core and/or pebble accretion, it is possible that K2-25b formed at large orbital distances where these models predict the creation of more massive planetary cores that later collided together to assemble a more massive planet. If K2-25b formed further out, it must have needed to migrate closer to the star to arrive at its current short $P = 3.48$ day orbit with its moderate eccentricity of $e = 0.428$. As such, K2-25b could still be in the process of migrating to an even shorter orbit through tidal migration and could represent a precursor of hot Neptunes seen around older stars. There are two major possibilities for migration of K2-25b: disk-driven and high-eccentricity migration.

Disk-driven migration (see, e.g., Kley & Nelson 2012, and references therein) relies on the exchange of angular momentum between the disk and the planet through mutual gravitational interactions within the plane of the disk. These interactions tend to migrate planets from long-period orbits to shorter-period orbits while damping eccentricities and thus resulting in circular orbits within the timescale of disk dissipation (Kley & Nelson 2012). Therefore, to explain K2-25b's current moderate eccentricity, a round of dynamical interactions would be needed. However, K2-25b's eccentricity
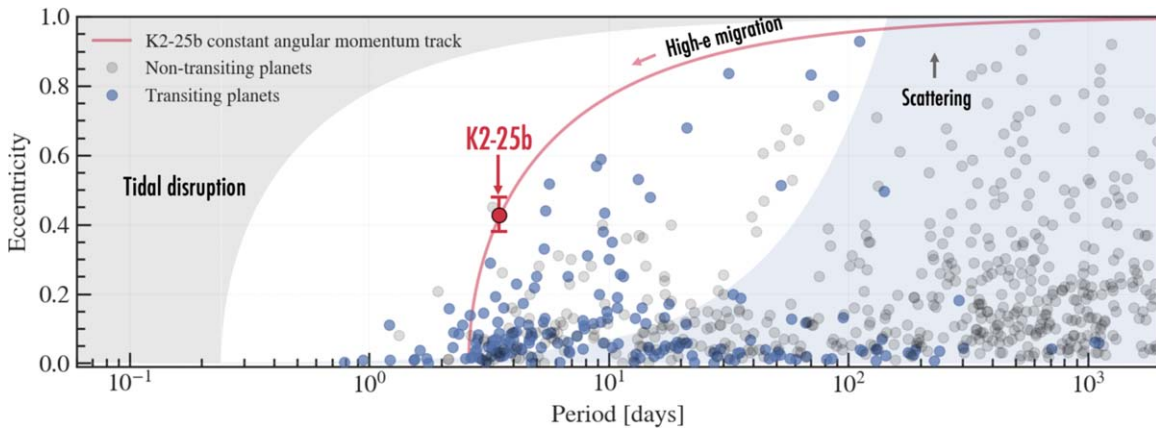
Figure 12. Eccentricity as a function of orbital period for known exoplanet systems; gray points show known nontransiting systems, and blue points show known transiting planets. The blue region shows the region where scattering tends to leads to eccentricity excitation rather than collisions (calculated assuming K2-25b's current mass of 25 $M_\oplus$). Seed planetary cores could have formed at these orbital distances and then scattered through gravitational interactions to a high-eccentricity orbit. Subsequently, K2-25b could have migrated closer to its host star via tidal interactions, arriving at its current orbit. The red curve shows the track of constant angular momentum for K2-25b, showing a possible migration pathway. Only systems with eccentricity errors less than <0.1 are shown.

is much larger than we expect from eccentricity excitation following migration (Petrovich et al. 2014).

Another possible scenario is that K2-25b arrived at its present orbit via high-eccentricity migration, a process that appears to be the dominant process for generating short-period giant planets (Dawson & Johnson 2018) and has been used to explain the migration process for most observed warm giants with $e > 0.4$ (Petrovich & Tremaine 2016). High-eccentricity migration can often be approximated as a two-step process: reducing the planet's orbital angular momentum and then reducing its energy (Dawson & Johnson 2018). During the first step, a perturber extracts orbital angular momentum from the planet by perturbing it into a highly elliptical orbit. In the second step, the planet tidally dissipates its orbital energy through interactions with the central star. If so, what originally excited K2-25b's eccentricity? Several theories have been proposed to explain the original excitation of eccentricities, including planet–planet scattering and/or merging events (Rasio & Ford 1996; Chatterjee et al. 2008; Jurić & Tremaine 2008), secular chaos (Wu & Lithwick 2011), and stellar flybys (e.g., Kaib et al. 2013). Additionally, secular interactions—e.g., via the von Zeipel–Lidov–Kozai mechanism from a widely separated perturber (Naoz 2016; Ito & Ohtsuka 2019) or coplanar secular interactions (Petrovich 2015) —can trigger high-eccentricity migration. However, significant spin–orbit misalignment and retrograde motion can result from the von Zeipel–Lidov–Kozai mechanism (e.g., Storch et al. 2017; Bourrier et al. 2018b). Therefore, to explain the observed low obliquity of K2-25b, we argue that this mechanism is less likely to be the cause of K2-25b's moderate eccentricity. Instead, to explain K2-25's low inferred obliquity, planet–planet scattering events and/or coplanar secular interactions are more likely mechanisms, as they can produce systems with high eccentricities but low inclinations (see, e.g., Chatterjee et al. 2008; Petrovich et al. 2014; Petrovich 2015).

Figure 12 compares the orbital eccentricities of exoplanets as a function of orbital period,[29] showing that K2-25b is among a select few planets with moderate eccentricities ($e > 0.4$) at short orbital periods (<10 days). The region to the right of the gray curve in Figure 12 is the region where planet–planet

scattering can take place to excite eccentricities and not preferentially cause collisions.[30] As discussed above, a possible formation scenario for K2-25b is that initial planet seed cores at the isolation mass formed via pebble accretion at long orbital periods, which then scattered via dynamical interactions to high eccentricities. These highly eccentric orbits then potentially led to orbit crossings and subsequent collisions resulting in the dense planet we see today, which could then be currently migrating toward a shorter circular orbit through tidal interactions with the star. Figure 12 highlights a nominal migration track assuming a track of constant angular momentum. Extrapolating this track suggests a fully circularized orbit with a period of ~2.5 days (see Figure 12).

Using tidal dissipation theory, we can gain further insight into the plausibility of this formation scenario. Tidal dissipation mechanisms vary strongly with the internal structure of the planet (Goldreich & Soter 1966; Guenel et al. 2014), with higher tidal quality factors Q seen for the gas giant planets than the denser rocky planets in the solar system (Goldreich & Soter 1966).[31] Using the equations in Jackson et al. (2009), Kain et al. (2020) estimated a circularization timescale of 410 Myr for K2-25b, assuming a modified tidal quality factor[32] of $Q_*' = 10^5$ for the host star and $Q_p' = 5 \times 10^4$ for K2-25b, which they selected based on Neptune's most likely Q_p' value from Zhang & Hamilton (2008). As further noted by Kain et al. (2020), the exact value of the tidal circularization timescale for K2-25b scales directly with Q_p'. Assuming the same tidal quality factors for the planet and the star as Kain et al. (2020) but using the planetary mass, radius, and a/R_* values derived in this work, we estimate a circularization timescale of 306 Myr, which is slightly lower but broadly consistent with their value. We formally require a tidal quality factor of $Q_p' > 1 \times 10^5$ to achieve a tidal circularization timescale

---

[29] Data obtained from the NASA Exoplanet Archive (Akeson et al. 2013).

[30] Calculated assuming K2-25b's current mass of ~25 $M_\oplus$ using Equation (10) in Dawson & Johnson (2018), which compares the escape velocity of the planet's surface to the escape velocity from the star at the planet's semimajor axis.

[31] The tidal quality factor Q is a factor quantifying the degree of tidal dissipation in gravitational systems and is inversely proportional to the degree of dissipation.

[32] The modified tidal quality factor Q' is defined as $3Q/2k_2$, where k_2 is the Love number of degree 2 (Goldreich & Soter 1966) for the system.

consistent with or longer than the age of the K2-25 system (650–800 Myr). If the tidal quality factor of K2-25b is indeed $Q'_p = 1 \times 10^5$ or larger, this could explain the moderate eccentricity of K2-25b we observe today, suggesting that at its current age of 650–800 Myr, K2-25b has not had sufficient time to circularize its orbit. Although larger than Neptune's quality factor, we note that it has been hypothesized that the interior structures of close-in Neptune-sized planets may differ from those of the more distant ice giants in our solar system; in particular, Morley et al. (2017) reported a high dissipation factor for GJ 436b of $Q'_p = 10^5$–10^6, which has been theorized to help explain the moderate eccentricity $e = 0.16$ observed for GJ 436b.

If, however, we assume a lower tidal quality of $Q'_p = 5 \times 10^3$—a representative tidal quality factor between the tidal quality factors of the rocky planets and the gas giants in the solar system (Goldreich & Soter 1966)—we obtain a circularization timescale of 30 Myr, which is substantially shorter than the age of the system (650–800 Myr). If the tidal quality factor is indeed this low, K2-25b would likely require additional ongoing eccentricity excitation to account for its currently observed moderate eccentricity. Although ongoing eccentricity excitation via Kozai–Lidov cycles is less likely given the low measured obliquity, coplanar secular excitation —as has been explored by Batygin et al. (2009) to account for the moderate eccentricity of GJ 436 b—is a possibility. However, as discussed in Section 8.5, we do not see any clear evidence for a second massive planetary companion in the HPF RVs, although more precision RVs are needed to confidently rule out the presence of smaller planets that could be present. Another, more fine-tuned possibility that we cannot rule out from the available data is that K2-25b was only recently (around 30 Myr ago) excited to an eccentric orbit far from the star and could then still be in the process of circularizing its orbit.

With a single transiting planet seen in the K2 data, K2-25b is consistent with the trend observed in Van Eylen et al. (2019) that single transiting planets tend to have higher eccentricities than planets in systems with multiple transiting planets, as well as the trend that Dong et al. (2018) observed that hot Neptunes —planets with 2–6 $R_\oplus$ and an orbital period $P < 10$ days—are most commonly found in single transiting systems. Further, Petigura et al. (2017) noted that more massive sub-Saturns tend to have moderately eccentric orbits and orbit stars without other detected planets. By detecting more young Neptune-sized systems, we can compare their observed properties (e.g., eccentricities and obliquities) and compare them to the predictions from different formation and migration mechanisms to start to establish a clearer picture of how short-period Neptune-sized planets originate.

8.7. Independent Analysis of K2-25b by IRD

During the preparation of this manuscript, we became aware that Gaidos et al. (2020) performed a complimentary analysis of the K2-25b system to constrain its obliquity using the IRD on the 8.2 m Subaru Telescope. Although the submissions of these complementary studies were coordinated between the groups, the data analyses and interpretations were performed independently.

9. Summary

We present the first mass and obliquity constraint for the young Neptune-sized planet K2-25b orbiting its M4.5 dwarf host star in the Hyades cluster. Given its known age and well-characterized orbital parameters, K2-25b is a benchmark system to study M dwarf planet formation and subsequent dynamics, giving us further insight into the formation and migration mechanisms that produce other hot Neptune exoplanets.

To characterize the planet properties, we jointly fit the available K2 photometry along with precision diffuser-assisted ground-based photometry obtained with the Engineered Diffuser on the ARCTIC imager on the 3.5 m telescope at APO and the newly installed Engineered Diffuser on the HDI on the 0.9 m WIYN Telescope at Kitt Peak Observatory, along with precision out-of-transit NIR RVs from the HPF spectrograph at the 10 m HET at McDonald Observatory. We see clear evidence for starspot activity in both the K2 data and HPF RVs and associated activity indicators. Jointly fitting the available photometry and RVs suggests a best-fit radius of $R = 3.44 \pm 0.12\ R_\oplus$, an eccentric orbit of $e = 0.41 \pm 0.05$, and a mass of $M = 24.5^{+5.7}_{-5.2}\ M_\oplus$. We tested the robustness of our HPF mass measurement by conducting injection-and-recovery tests in synthetic RV streams. Using our radius and mass constraints and assuming a two-component composition model of a rocky core enshrouded by a thin H/He envelope, we obtain an H/He envelope mass fraction of 5%. No obvious long-period massive companion is detected in the HPF RV data, and continued precise RV monitoring is required to confidently detect or exclude such a companion.

To constrain the obliquity of the system, we present three RM effect observations of K2-25b obtained with HPF, yielding a sky-projected obliquity constraint of $\lambda = 3° \pm 16°$. Using our constraint for the stellar inclination derived from the stellar radius and our $v \sin i_* = 8.8 \pm 0.6$ km s^{-1} constraint from the high-resolution HPF spectra, we obtain a true 3D obliquity of $\psi = 17^{+11}_{-8}°$. Our obliquity and eccentricity constraints paint a picture of a well-aligned but eccentric system.

With precisely determined age and orbital parameters, we discuss a few possible formation scenarios for K2-25b. If K2-25b reached its current mass during the gas disk phase beyond the ice line, it would be at odds with the predictions of core- and pebble-accretion models—with certain assumptions about the disk properties and planetesimal accretion luminosity—as those models predict that K2-25b should have experienced runaway gas accretion resulting in a gas giant planet. To explain its currently observed mass, we surmise that K2-25b could be the product of planet merging events of smaller planetary cores to produce a more massive planet. Such a dynamical environment could have excited K2-25b into an eccentric orbit, and K2-25b could be in the process of migrating to a shorter-period orbit through tidal interactions with the host star. To explain K2-25b's current moderate eccentricity from tidal circularization theory, we place a lower limit on the tidal quality factor of $Q'_p \sim 10^5$, corresponding to a circularization timescale consistent with the age of the system. This tidal quality factor is higher than the tidal quality factor for Neptune, which suggest that K2-25b's internal structure could be different from that of the small gas giants (Uranus, Neptune) in the solar system.

Facilities: K2, Gaia, HDI/WIYN 0.9 m, ARCTIC/ARC 3.5 m, HPF/HET 10 m.

Software: AstroImageJ (Collins et al. 2017), astroplan (Morris et al. 2018), astropy (Astropy Collaboration et al. 2013), astroquery (Ginsburg et al. 2018), barycorrpy (Kanodia & Wright 2018), batman (Kreidberg 2015), corner.py (Foreman-Mackey 2016), celerite (Foreman-Mackey et al. 2017), dynesty (Speagle 2020), emcee (Foreman-Mackey et al. 2013), everest (Luger et al. 2018), EXOFASTv2 (Eastman 2017), HxRGproc (Ninan et al. 2018), iDiffuse (Stefansson et al. 2018b), Jupyter (Kluyver et al. 2016), juliet (Espinoza et al. 2019), matplotlib (Hunter 2007), numpy (Van Der Walt et al. 2011), MRExo (Kanodia et al. 2019), pandas (McKinney 2010), PyAstronomy (Czesla et al. 2019), pyde (Parviainen 2016), radvel (Fulton et al. 2018), SERVAL (Zechmeister et al. 2018).

Appendix A
Calcium IRT Line Positions

Table A1 lists the line index positions used to measure the Ca II IRT indices in the HPF spectra.

Table A1
Line Index Positions Used for Ca II IRT Activity Indicators

Line No.	Description	Start and End Wavelengths (Å)
1	Line center	[8499.930, 8500.780]
1	Left reference region	[8493.200, 8495.467]
1	Right reference region	[8505.202, 8507.472]
2	Line center	[8544.009, 8544.864]
2	Left reference region	[8535.887, 8538.737]
2	Right reference region	[8551.562, 8554.412]
3	Line center	[8664.086, 8664.953]
3	Left reference region	[8657.294, 8660.184]
3	Right reference region	[8670.300, 8673.190]

Note. Wavelengths are given in vacuum wavelengths.

Appendix B
Injection and Recovery Tests

Table B1 and Figures B1 and B2 summarize the results from our two series (tests I and II) of synthetic injection and recovery tests. The methodology is further described in Section 6.4. Figures B1 and B2 show that the injected Keplerian parameters are consistently accurately recovered.
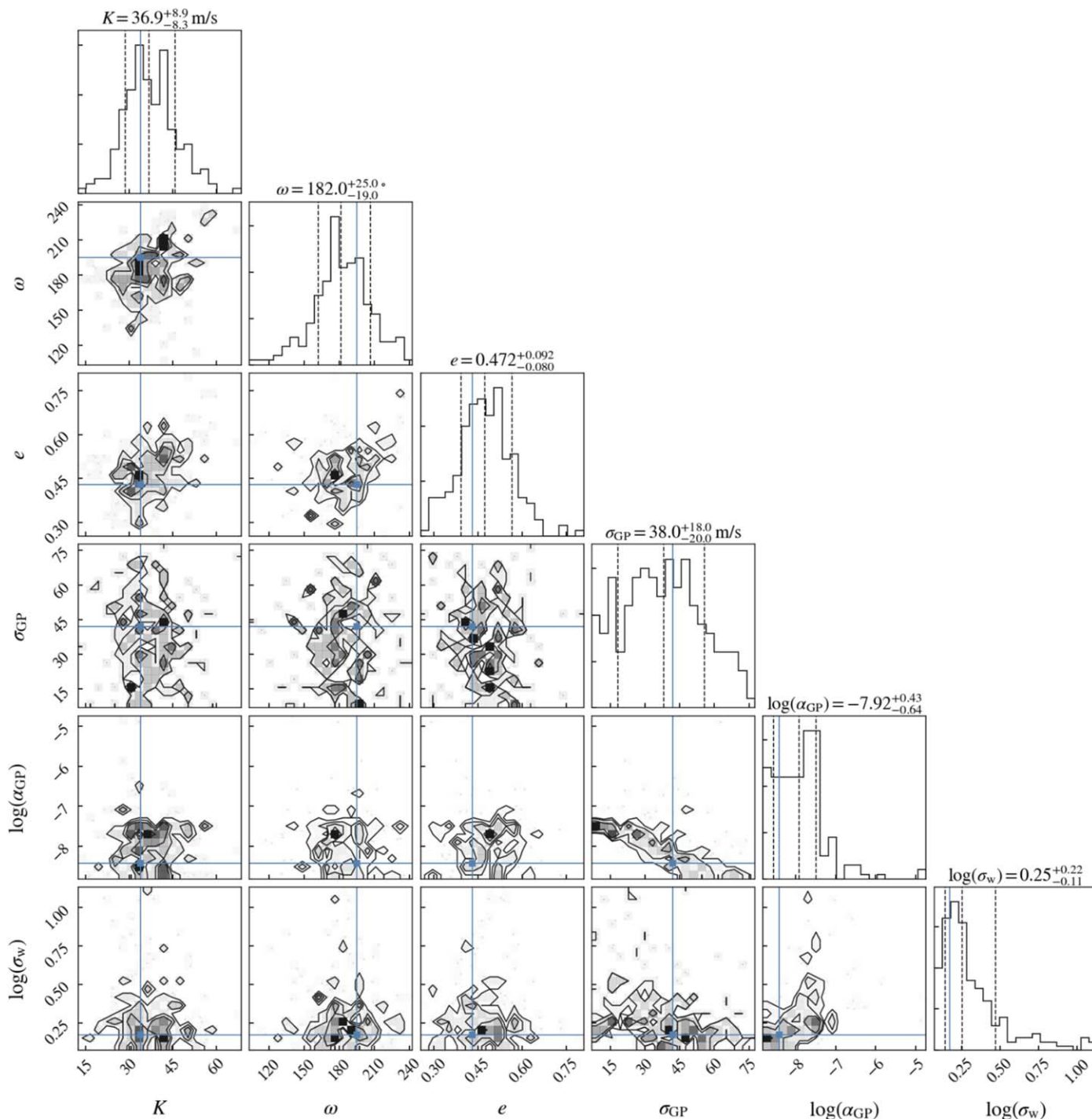
Figure B1. Injection and recovery test I: results of 200 injection and recovery tests in synthetic HPF RV streams. The panels show the distribution of the means of individual posteriors. The known injected values are highlighted with blue lines. The distribution of mean values agrees well with the known values. Plot generated using `corner.py` (Foreman-Mackey 2016).
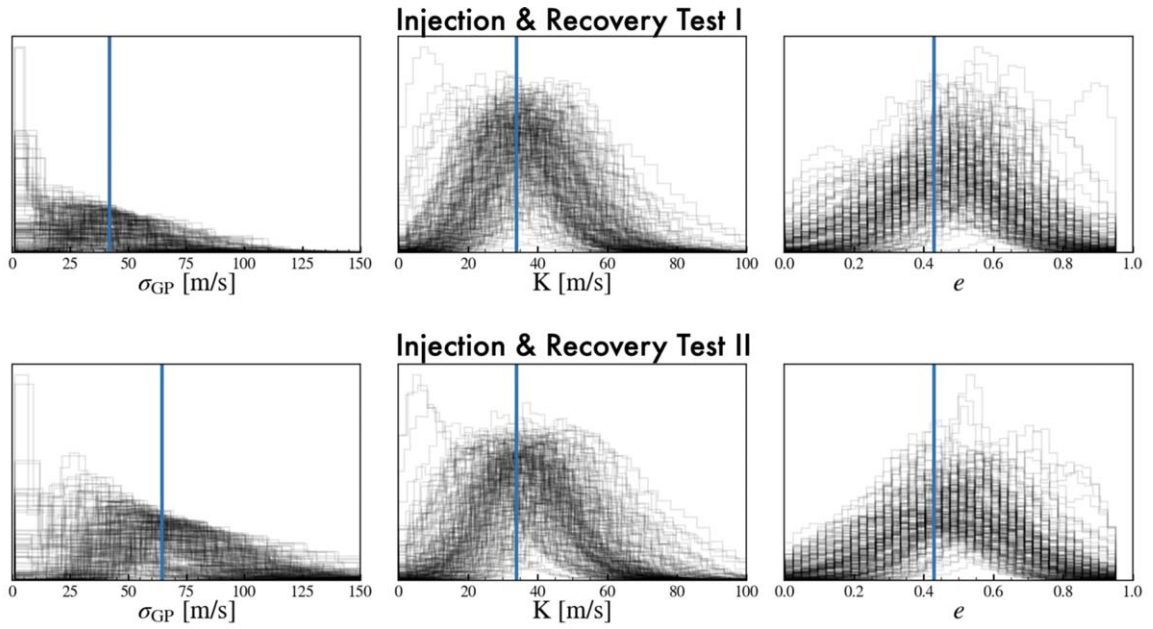
Figure B2. Posteriors (black curves; 200 each) of the GP amplitude $\sigma_{\rm GP}$, RV semiamplitude K, and eccentricity e after two series of 200 injection and recovery tests in the HPF out-of-transit RVs. True values for $\sigma_{\rm GP}$, K, and e are indicated by blue lines. The first test (test I; top panels) set $\sigma_{\rm GP} = 42$ m s^{-1}, $K = 34$ m s^{-1}, and $e = 0.43$, similar to the nominal median expected values from fit RV2. The true value of the semiamplitude is within the 68% and 95% credible intervals in 80% and 99.7% of the cases, respectively. The second test (test II; bottom panels) assumed that $\sigma_{\rm GP} = 64.6$ m s^{-1}, or at the 95th quantile value from fit RV2, while keeping the other parameters the same. Even with the higher assumed correlated noise, the true value of the semiamplitude is still reliably recovered at a high coverage probability; the true value of the semiamplitude is within the 68% and 95% credible intervals in 75% and 97% of the cases, respectively.

Table B1
Summary of Injected Parameters for Both Series of Tests Considered

Parameter	Description	Prior	Value: Test 1	Value: Test 2
Keplerian Parameters				
P (days)	Orbital period	$\mathcal{N}(3.484548, 0.000042)$	3.48456424	
T_C	Transit midpoint–2,400,000 (BJD$_{\rm TDB}$)	$\mathcal{U}(58515.63, 58515.66)$	58,515.642096	
e	Eccentricity	$\mathcal{U}(0, 0.95)$	0.43	
ω	Argument of periastron	$\mathcal{U}(0, 360)$	195	
K	RV semiamplitude (m s^{-1})	$\mathcal{U}(0, 200)$	34	
GP Hyperparameters				
$P_{\rm GP}$	GP period (days)	$\mathcal{N}(1.8784, 0.005)$	1.88178	
$\sigma_{\rm GP}$	RV GP amplitude (m s^{-1})	$\mathcal{U}(10^1, 10^5)$	42	64.6
$\Gamma_{\rm GP}$	Harmonic structure/scaling parameter	$\mathcal{N}(8.0, 1.9)$	7.4	
$\alpha_{\rm GP}$	Inverse length scale (day^{-2})	$\mathcal{J}(10^{-12}, 10^{-3})$	3.8×10^{-9}	
Other HPF Parameters				
$\sigma_{\rm w}$	HPF white-noise RV jitter (m s^{-1})	$\mathcal{J}(0.1, 300)$	1.5	
$\mu_{\rm HPF}$	HPF RV offset (m s^{-1})	$\mathcal{U}(-200, 200)$	0	

Note. The results from the injection and recovery test are summarized in Figures B1 and B2. Here $\mathcal{N}(m, \sigma)$ denotes a normal prior with mean m and standard deviation σ, $\mathcal{U}(a, b)$ denotes a uniform prior with a start value a and end value b, and $\mathcal{J}(a, b)$ denotes a Jeffreys prior with a start value a and end value b.

Appendix C
HPF RVs

C.1. Out of Transit

Table C1 lists the RVs from HPF used for the mass measurement of K2-25b, along with associated stellar activity indicators.

C.2. In Transit

Table C2 lists the RVs from HPF used for the RM effect analysis. These RVs had an exposure time of 300 s.

Table C1
Out-of-transit RVs from HPF Along with the dLW, CRX, and Line Indices for the Three Ca II IRT Lines (Ca II IRT 1, 2, and 3) and Associated Errors

BJD	RV (m s^{-1})	dLW (m^2 s^{-2})	CRX (m s^{-1} Np^{-1})	Ca II IRT 1	Ca II IRT 2	Ca II IRT 3
2,458,424.95976	29.8 ± 15.6	288.7 ± 74.2	88.1 ± 233.7	0.878 ± 0.005	0.790 ± 0.006	0.662 ± 0.005
2,458,425.74905	−90.6 ± 35.6	312.2 ± 170.0	−1649.2 ± 478.6	1.097 ± 0.014	0.931 ± 0.017	0.828 ± 0.013
2,458,429.93716	39.5 ± 16.8	64.9 ± 80.0	−445.4 ± 209.2	0.930 ± 0.006	0.826 ± 0.007	0.703 ± 0.005
2,458,433.92567	44.7 ± 38.0	311.3 ± 180.5	1049.5 ± 630.4	0.854 ± 0.012	0.764 ± 0.016	0.685 ± 0.012
2,458,436.91691	−56.8 ± 23.9	−266.8 ± 114.7	−145.4 ± 332.6	0.975 ± 0.008	0.871 ± 0.010	0.708 ± 0.008
2,458,437.90840	18.0 ± 17.3	88.2 ± 82.9	317.4 ± 224.3	1.045 ± 0.006	0.926 ± 0.008	0.776 ± 0.006
2,458,439.91091	−5.9 ± 21.2	301.2 ± 101.1	174.7 ± 394.9	0.908 ± 0.007	0.801 ± 0.009	0.686 ± 0.007
2,458,441.89899	62.8 ± 22.3	176.8 ± 106.5	−132.8 ± 183.3	0.893 ± 0.007	0.784 ± 0.009	0.668 ± 0.007
2,458,442.89348	−28.7 ± 29.1	123.3 ± 139.4	437.9 ± 522.9	0.988 ± 0.010	0.882 ± 0.012	0.760 ± 0.009
2,458,443.71423	38.9 ± 24.4	296.1 ± 116.1	19.8 ± 352.8	0.908 ± 0.007	0.810 ± 0.009	0.712 ± 0.007
2,458,444.71135	39.9 ± 19.6	−315.5 ± 94.6	34.1 ± 181.4	0.946 ± 0.006	0.844 ± 0.008	0.720 ± 0.006
2,458,449.88697	−80.4 ± 22.3	169.7 ± 107.3	−236.0 ± 321.6	0.970 ± 0.007	0.876 ± 0.009	0.761 ± 0.007
2,458,451.68266	−19.1 ± 28.1	319.9 ± 134.9	387.9 ± 453.2	0.900 ± 0.009	0.859 ± 0.012	0.713 ± 0.009
2,458,473.80425	−4.4 ± 42.5	1752.3 ± 196.0	178.1 ± 669.2	0.893 ± 0.015	0.762 ± 0.019	0.644 ± 0.014
2,458,480.80404	21.5 ± 52.9	43.1 ± 252.9	127.4 ± 632.2	0.860 ± 0.020	0.744 ± 0.027	0.635 ± 0.021
2,458,487.78924	−153.6 ± 44.8	−523.5 ± 218.1	137.8 ± 710.1	0.891 ± 0.017	0.718 ± 0.024	0.640 ± 0.017
2,458,546.61407	1.0 ± 33.4	−390.2 ± 162.4	434.9 ± 462.0	0.895 ± 0.010	0.829 ± 0.013	0.677 ± 0.010
2,458,549.60481	15.6 ± 28.0	473.1 ± 134.3	−178.2 ± 444.0	0.885 ± 0.008	0.825 ± 0.011	0.684 ± 0.008
2,458,741.89127	−36.4 ± 37.6	−179.1 ± 180.4	−55.6 ± 587.0	0.907 ± 0.012	0.831 ± 0.017	0.708 ± 0.012
2,458,744.87566	11.1 ± 31.4	−48.3 ± 149.9	−1098.4 ± 405.1	1.040 ± 0.011	0.960 ± 0.014	0.823 ± 0.010
2,458,752.85672	−43.7 ± 31.5	393.2 ± 149.1	−267.1 ± 441.1	1.030 ± 0.011	0.907 ± 0.015	0.803 ± 0.011
2,458,804.90940	−107.8 ± 41.2	486.7 ± 196.0	1583.8 ± 570.3	0.902 ± 0.014	0.801 ± 0.018	0.667 ± 0.014
2,458,805.71647	−117.9 ± 28.5	433.8 ± 135.7	−1673.7 ± 264.1	0.874 ± 0.010	0.753 ± 0.013	0.674 ± 0.010
2,458,808.70580	7.6 ± 23.4	−300.2 ± 112.8	64.8 ± 464.9	0.946 ± 0.008	0.889 ± 0.011	0.726 ± 0.008
2,458,808.90127	31.0 ± 22.0	−61.7 ± 105.8	−96.6 ± 260.6	1.024 ± 0.008	0.921 ± 0.010	0.775 ± 0.007
2,458,811.88979	28.6 ± 30.4	−132.5 ± 146.7	−412.6 ± 421.3	0.918 ± 0.010	0.859 ± 0.013	0.708 ± 0.010
2,458,824.66447	−97.2 ± 44.0	722.8 ± 209.6	247.7 ± 747.0	0.907 ± 0.015	0.797 ± 0.020	0.677 ± 0.015
2,458,825.66903	32.9 ± 55.7	−289.9 ± 271.4	365.9 ± 792.5	0.939 ± 0.018	0.878 ± 0.024	0.757 ± 0.018
2,458,832.64612	58.1 ± 35.4	−230.3 ± 172.1	738.2 ± 645.5	0.899 ± 0.011	0.792 ± 0.015	0.692 ± 0.012
2,458,849.59344	39.7 ± 54.1	254.3 ± 256.9	616.0 ± 873.0	0.907 ± 0.017	0.774 ± 0.021	0.714 ± 0.017
2,458,849.77940	41.6 ± 32.7	−606.0 ± 158.7	661.1 ± 496.7	0.924 ± 0.010	0.817 ± 0.013	0.683 ± 0.010
2,458,852.77670	−61.7 ± 27.8	271.2 ± 132.7	−400.7 ± 457.1	0.901 ± 0.008	0.821 ± 0.011	0.675 ± 0.008

(This table is available in machine-readable form.)

Table C2
In-transit RVs from HPF

Time (BJD$_{\rm TDB}$)	RV (m s^{-1})	RV Error (m s^{-1})	S/N	Transit No.
2,458,473.798377	21.502	92.473	31.5	1
2,458,473.802296	−99.316	85.383	32.9	1
2,458,473.806148	32.915	87.976	33.0	1
2,458,473.810188	25.879	76.650	36.0	1
2,458,473.814183	58.845	68.489	38.9	1
2,458,473.818066	22.483	81.288	35.4	1
2,458,473.822004	−29.955	70.497	38.1	1
2,458,473.825933	−107.874	82.864	33.7	1
2,458,473.829840	10.968	101.494	28.8	1
2,458,473.833884	5.058	112.039	26.2	1
2,458,473.837847	−5.540	111.578	26.1	1
2,458,480.779096	93.172	81.592	32.5	2
2,458,480.783031	84.061	74.764	35.2	2
2,458,480.786978	289.359	70.453	36.9	2
2,458,480.790926	118.139	59.718	42.5	2
2,458,480.794850	147.978	61.526	41.0	2
2,458,480.798729	−91.458	63.679	40.3	2
2,458,480.802696	−89.542	72.040	36.7	2
2,458,480.806659	−88.708	71.505	36.4	2
2,458,480.810610	82.751	78.649	34.5	2
2,458,480.814557	−30.039	93.241	29.1	2
2,458,480.818470	−30.570	103.872	27.2	2
2,458,487.763970	−32.264	92.523	29.1	3
2,458,487.767653	−108.714	72.947	35.5	3
2,458,487.771528	−163.954	69.931	37.3	3
2,458,487.775525	−131.220	67.386	38.7	3
2,458,487.779335	−91.287	66.037	38.8	3
2,458,487.783313	−202.220	74.173	35.5	3
2,458,487.787296	−203.813	88.859	30.1	3
2,458,487.791204	−20.690	97.731	28.4	3
2,458,487.795138	−138.737	108.448	25.3	3

(This table is available in machine-readable form.)

ORCID iDs

Gudmundur Stefansson ⬚ https://orcid.org/0000-0001-7409-5688

Suvrath Mahadevan ⬚ https://orcid.org/0000-0001-9596-7983

Marissa Maney ⬚ https://orcid.org/0000-0001-8222-9586

Joe P. Ninan ⬚ https://orcid.org/0000-0001-8720-5612

Paul Robertson ⬚ https://orcid.org/0000-0003-0149-9678

Lori Allen ⬚ https://orcid.org/0000-0002-7789-5119

Eric B. Ford ⬚ https://orcid.org/0000-0001-6545-639X

Joshua Winn ⬚ https://orcid.org/0000-0002-4265-047X

Angie Wolfgang ⬚ https://orcid.org/0000-0003-2862-6278

Rebekah I. Dawson ⬚ https://orcid.org/0000-0001-9677-1296

John Wisniewski ⬚ https://orcid.org/0000-0001-9209-1808

Chad F. Bender ⬚ https://orcid.org/0000-0003-4384-7220

Caleb Cañas ⬚ https://orcid.org/0000-0003-4835-0619

William Cochran ⬚ https://orcid.org/0000-0001-9662-3496

Leslie Hebb ⬚ https://orcid.org/0000-0003-1263-8637

Shubham Kanodia ⬚ https://orcid.org/0000-0001-8401-4300

Andrew J. Metcalf ⬚ https://orcid.org/0000-0001-5000-1018

Arpita Roy ⬚ https://orcid.org/0000-0001-8127-5775

Christian Schwab ⬚ https://orcid.org/0000-0002-0091-7105

Ryan Terrien ⬚ https://orcid.org/0000-0002-4788-8858

Jason T. Wright ⬚ https://orcid.org/0000-0001-6160-5888

References

Adams, E. R., Seager, S., & Elkins-Tanton, L. 2008, ApJ, 673, 1160
Addison, B. C., Horner, J., Wittenmyer, R. A., et al. 2020, arXiv:2006.13675
Akaike, H. 1974, ITAC, 19, 716
Akeson, R. L., Chen, X., Ciardi, D., et al. 2013, PASP, 125, 989
Albrecht, S., Winn, J. N., Johnson, J. A., et al. 2012, ApJ, 757, 18
Ambikasaran, S., Foreman-Mackey, D., Greengard, L., Hogg, D. W., & O'Neil, M. 2015, ITPAM, 38, 252
Anglada-Escudé, G., & Butler, R. P. 2012, ApJS, 200, 15
Angus, R., Morton, T., Aigrain, S., Foreman-Mackey, D., & Rajpaul, V. 2018, MNRAS, 474, 2094
Artigau, É, Kouach, D., Donati, J.-F., et al. 2014, Proc. SPIE, 9147, 914715
Astropy Collaboration, Robitaille, T. P., Tollerud, E. J., et al. 2013, A&A, 558, A33
Awiphan, S., Kerins, E., Pichadee, S., et al. 2016, MNRAS, 463, 2574
Barragán, O., Aigrain, S., Kubyshkina, D., et al. 2019, MNRAS, 490, 698
Batalha, N. E., Mandell, A., Pontoppidan, K., et al. 2017, PASP, 129, 064501
Batygin, K., Bodenheimer, P. H., & Laughlin, G. P. 2016, ApJ, 829, 114
Batygin, K., Laughlin, G., Meschiari, S., et al. 2009, ApJ, 699, 23
Benatti, S., Nardiello, D., Malavolta, L., et al. 2019, A&A, 630, A81
Bitsch, B., Morbidelli, A., Johansen, A., et al. 2018, A&A, 612, A30
Bodenheimer, P., & Pollack, J. B. 1986, Icar, 67, 391
Bourrier, V., Lecavelier Des Etangs, A., Ehrenreich, D., et al. 2018a, A&A, 620, A147
Bourrier, V., Lovis, C., Beust, H., et al. 2018b, Natur, 553, 477
Bowler, B. P., Blunt, S. C., & Nielsen, E. L. 2020, AJ, 159, 63
Burgasser, A. J., & Mamajek, E. E. 2017, ApJ, 845, 110
Chatterjee, S., Ford, E. B., Matsumura, S., & Rasio, F. A. 2008, ApJ, 686, 580
Chen, J., & Kipping, D. 2017, ApJ, 834, 17
Claudi, R., Benatti, S., Carleo, I., et al. 2018, Proc. SPIE, 10702, 107020Z

Collins, K. A., Kielkopf, J. F., Stassun, K. G., & Hessman, F. V. 2017, AJ, 153, 77

Crossfield, I. J. M., & Kreidberg, L. 2017, AJ, 154, 261

Cutri, R. M., Skrutskie, M. F., van Dyk, S., et al. 2003, yCat, 2246, 0

Cutri, R. M., Wright, E. L., Conrow, T., et al. 2014, yCat, 2328, 0

Czesla, S., Schröter, S., Schneider, C. P., et al. 2019, PyA: Python Astronomy-related Packages, version 0.10.1, Astrophysics Source Code Library, ascl:1906.010

Dai, F., Winn, J. N., Gandolfi, D., et al. 2017, AJ, 154, 226

David, T. J., Conroy, K. E., Hillenbrand, L. A., et al. 2016, AJ, 151, 112

David, T. J., Petigura, E. A., Luger, R., et al. 2019, ApJL, 885, L12

Dawson, R. I., & Johnson, J. A. 2012, ApJ, 756, 122

Dawson, R. I., & Johnson, J. A. 2018, ARA&A, 56, 175

Deliyannis, C. P. 2013, AAS Meeting, 222, 111.06

Dmitrienko, E. S., & Savanov, I. S. 2017, ARep, 61, 871

Dodson-Robinson, S. E., Veras, D., Ford, E. B., & Beichman, C. A. 2009, ApJ, 707, 79

Dong, S., Xie, J.-W., Zhou, J.-L., Zheng, Z., & Luo, A. 2018, PNAS, 115, 266

Dressing, C. D., & Charbonneau, D. 2015, ApJ, 807, 45

Eastman, J. 2017, EXOFASTv2: Generalized Publication-quality Exoplanet Modeling Code, v2, Astrophysics Source Code Library, ascl:1710.003

Eastman, J. D., Rodriguez, J. E., Agol, E., et al. 2019, arXiv:1907.09480

Ehrenreich, D., Bourrier, V., Wheatley, P. J., et al. 2015, Natur, 522, 459

Espinoza, N. 2018, RNAAS, 2, 209

Espinoza, N., Kossakowski, D., & Brahm, R. 2019, MNRAS, 490, 2262

Fabrycky, D., & Tremaine, S. 2007, ApJ, 669, 1298

Fischer, D. A., Anglada-Escude, G., Arriagada, P., et al. 2016, PASP, 128, 066001

Foreman-Mackey, D. 2016, JOSS, 24, 1

Foreman-Mackey, D., Agol, E., Ambikasaran, S., & Angus, R. 2017, AJ, 154, 220

Foreman-Mackey, D., Hogg, D. W., Lang, D., & Goodman, J. 2013, PASP, 125, 306

Fulton, B. J., Petigura, E. A., Blunt, S., & Sinukoff, E. 2018, PASP, 130, 044504

Gaia Collaboration 2018, yCat, 1345, 0

Gaidos, E., Hirano, T., Wilson, D. J., et al. 2020, MNRAS, 498, L119

Gibson, S. R., Howard, A. W., Marcy, G. W., et al. 2016, Proc. SPIE, 9908, 990870

Ginsburg, A., Sipocz, B., Parikh, M., et al. 2018, astropy/astroquery: v0.3.7 Release, Zenodo, doi:10.5281/zenodo.1160627

Goldreich, P., & Sari, R. 2003, ApJ, 585, 1024

Goldreich, P., & Soter, S. 1966, Icar, 5, 375

González Hernández, J. I., Pepe, F., Molaro, P., & Santos, N. C. 2018, in Handbook of Exoplanets, ed. H. Deeg & J. Belmonte (Cham: Springer), 157

Grunblatt, S. K., Howard, A. W., & Haywood, R. D. 2015, ApJ, 808, 127

Guenel, M., Mathis, S., & Remus, F. 2014, A&A, 566, L9

Hardegree-Ullman, K. K., Cushing, M. C., Muirhead, P. S., & Christiansen, J. L. 2019, AJ, 158, 75

Haywood, R. D., Collier Cameron, A., Queloz, D., et al. 2014, MNRAS, 443, 2517

Haywood, R. D., Vanderburg, A., Mortier, A., et al. 2018, AJ, 155, 203

Hearty, F., Levi, E., Nelson, M., et al. 2014, Proc. SPIE, 9147, 914752

Henden, A. A., Levine, S., Terrell, D., & Welch, D. L. 2015, AAS Meeting, 225, 336.16

Hirano, T., Dai, F., Livingston, J. H., et al. 2018, AJ, 155, 124

Hirano, T., Gaidos, E., Winn, J. N., et al. 2020a, ApJL, 890, L27

Hirano, T., Krishnamurthy, V., Gaidos, E., et al. 2020b, ApJL, 899, L13

Hirano, T., Suto, Y., Taruya, A., et al. 2010, ApJ, 709, 458

Hirano, T., Suto, Y., Winn, J. N., et al. 2011, ApJ, 742, 69

Howell, S. B., Sobeck, C., Haas, M., et al. 2014, PASP, 126, 398

Huber, D., Bryson, S. T., Haas, M. R., et al. 2016, ApJS, 224, 2

Huehnerhoff, J., Ketzeback, W., Bradley, A., et al. 2016, Proc. SPIE, 9908, 99085H

Hunter, J. D. 2007, CSE, 9, 90

Inamdar, N. K., & Schlichting, H. E. 2015, MNRAS, 448, 1751

Irwin, J. M., Berta-Thompson, Z. K., Charbonneau, D., et al. 2015, in 18th Cambridge Workshop on Cool Stars, Stellar Systems, and the Sun, ed. G. van Belle & H. C. Harris (Flagstaff, AZ: Lowell Observatory), 767

Ito, T., & Ohtsuka, K. 2019, MEEP, 7, 1

Jackson, B., Barnes, R., & Greenberg, R. 2009, ApJ, 698, 1357

Johnson, J. A., Aller, K. M., Howard, A. W., & Crepp, J. R. 2010, PASP, 122, 905

Jurić, M., & Tremaine, S. 2008, ApJ, 686, 603

Kaib, N. A., Raymond, S. N., & Duncan, M. 2013, Natur, 493, 381

Kain, I. J., Newton, E. R., Dittmann, J. A., et al. 2020, AJ, 159, 83

Kanodia, S., Wolfgang, A., Stefansson, G. K., Ning, B., & Mahadevan, S. 2019, ApJ, 882, 38

Kanodia, S., & Wright, J. 2018, RNAAS, 2, 4

Kaplan, K. F., Bender, C. F., Terrien, R., et al. 2018, in ASP Conf. Ser. 523, Astronomical Data Analysis Software and Systems XXVIII, ed. P. J. Teuben et al. (San Fransisco, CA: ASP), 567

Kempton, E. M.-R., Bean, J. L., Louie, D. R., et al. 2018, PASP, 130, 114401

Kipping, D. M. 2010, MNRAS, 408, 1758

Kipping, D. M. 2013, MNRAS, 435, 2152

Klein, B., & Donati, J. F. 2020, MNRAS, 493, L92

Kley, W., & Nelson, R. P. 2012, ARA&A, 50, 211

Kluyver, T., Ragan-Kelley, B., Pérez, F., et al. 2016, in Positioning and Power in Academic Publishing: Players, Agents and Agendas, ed. F. Loizides & B. Scmidt (Amsterdam: IOS Press), 87

Kotani, T., Tamura, M., Nishikawa, J., et al. 2018, Proc. SPIE, 10702, 1070211

Kraft, R. P. 1967, ApJ, 150, 551

Kreidberg, L. 2015, PASP, 127, 1161

Lambrechts, M., & Johansen, A. 2012, A&A, 544, A32

Lambrechts, M., Johansen, A., & Morbidelli, A. 2014, A&A, 572, A35

Lambrechts, M., & Lega, E. 2017, A&A, 606, A146

Lee, E. J., Chiang, E., & Ormel, C. W. 2014, ApJ, 797, 95

Lépine, S., & Shara, M. M. 2005, AJ, 129, 1483

Liu, B., Lambrechts, M., Johansen, A., & Liu, F. 2019, A&A, 632, A7

Lopez, E. D., & Fortney, J. J. 2014, ApJ, 792, 1

López-Morales, M., Haywood, R. D., Coughlin, J. L., et al. 2016, AJ, 152, 204

Luger, R., Agol, E., Kruse, E., et al. 2016, AJ, 152, 100

Luger, R., Kruse, E., Foreman-Mackey, D., Agol, E., & Saunders, N. 2018, AJ, 156, 99

MacDonald, M. G., Dawson, R. I., Morrison, S. J., Lee, E. J., & Khandelwal, A. 2020, ApJ, 891, 20

Maciejewski, G., Niedzielski, A., Nowak, G., et al. 2014, AcA, 64, 323

Mahadevan, S., Ramsey, L., Bender, C., et al. 2012, Proc. SPIE, 8446, 84461S

Mahadevan, S., Ramsey, L. W., Terrien, R., et al. 2014, Proc. SPIE, 9147, 91471G

Mann, A. W., Dupuy, T., Kraus, A. L., et al. 2019, ApJ, 871, 63

Mann, A. W., Feiden, G. A., Gaidos, E., Boyajian, T., & von Braun, K. 2015, ApJ, 804, 64

Mann, A. W., Gaidos, E., Mace, G. N., et al. 2016a, ApJ, 818, 46

Mann, A. W., Gaidos, E., Vanderburg, A., et al. 2017, AJ, 153, 64

Mann, A. W., Newton, E. R., Rizzuto, A. C., et al. 2016b, AJ, 152, 61

Marcus, R. A., Sasselov, D., Hernquist, L., & Stewart, S. T. 2010, ApJL, 712, L73

Masuda, K., & Winn, J. N. 2020, AJ, 159, 81

Mazeh, T., Perets, H. B., McQuillan, A., & Goldstein, E. S. 2015, ApJ, 801, 3

McKinney, W. 2010, in Proc. 9th Python in Science Conf., ed. S. van der Walt & J. Millman (Austin, TX: SciPy), 56

McLaughlin, D. B. 1924, ApJ, 60, 22

Metcalf, A. J., Anderson, T., Bender, C. F., et al. 2019, Optica, 6, 233

Montet, B. T., Feinstein, A. D., Luger, R., et al. 2020, AJ, 159, 112

Morley, C. V., Knutson, H., Line, M., et al. 2017, AJ, 153, 86

Morris, B. M., Tollerud, E., Sipőcz, B., et al. 2018, AJ, 155, 128

Naoz, S. 2016, ARA&A, 54, 441

Nelson, B. E., Ford, E. B., Buchner, J., et al. 2020, AJ, 159, 73

Newton, E. R., Mann, A. W., Tofflemire, B. M., et al. 2019, ApJL, 880, L17

Ninan, J. P., Bender, C. F., Mahadevan, S., et al. 2018, Proc. SPIE, 10709, 107092U

Ninan, J. P., Mahadevan, S., Stefansson, G., et al. 2019, JATIS, 5, 041511

Palle, E., Oshagh, M., Casasayas-Barris, N., et al. 2020, arXiv:2006.13609

Parviainen, H. 2016, PyDE:v1.5, Zenodo, doi:10.5281/zenodo.45602

Pepper, J., Gillen, E., Parviainen, H., et al. 2017, AJ, 153, 177

Petigura, E. A., Sinukoff, E., Lopez, E. D., et al. 2017, AJ, 153, 142

Petrovich, C. 2015, ApJ, 805, 75

Petrovich, C., & Tremaine, S. 2016, ApJ, 829, 132

Petrovich, C., Tremaine, S., & Rafikov, R. 2014, ApJ, 786, 101

Plavchan, P., Barclay, T., Gagné, J., et al. 2020, Natur, 497, 582

Pollack, J. B., Hubickyj, O., Bodenheimer, P., et al. 1996, Icar, 124, 62

Quirrenbach, A., Amado, P. J., Ribas, I., et al. 2018, Proc. SPIE, 10702, 107020W

Rabus, M., Lachaume, R., Jordán, A., et al. 2019, MNRAS, 484, 2674

Rafikov, R. R. 2006, ApJ, 648, 666

Rafikov, R. R. 2011, ApJ, 727, 86

Rasio, F. A., & Ford, E. B. 1996, Sci, 274, 954

Reid, I. N., Cruz, K. L., Allen, P., et al. 2004, AJ, 128, 463

Reiners, A., Joshi, N., & Goldman, B. 2012, AJ, 143, 93

Ribas, Á., Bouy, H., & Merín, B. 2015, A&A, 576, A52

Ricker, G. R., Winn, J. N., Vanderspek, R., et al. 2014, Proc. SPIE, 9143, 914320

Rossiter, R. A. 1924, ApJ, 60, 15

Schlaufman, K. C. 2010, ApJ, 719, 602

Seifahrt, A., Bean, J. L., Stürmer, J., et al. 2016, Proc. SPIE, 9908, 990818

Shetrone, M., Cornell, M. E., Fowler, J. R., et al. 2007, PASP, 119, 556

Shporer, A. 2017, PASP, 129, 072001

Southworth, J. 2011, MNRAS, 417, 2166

Speagle, J. S. 2020, MNRAS, 493, 3132

Stefansson, G., Cañas, C., Wisniewski, J., et al. 2020, AJ, 159, 100

Stefansson, G., Hearty, F., Robertson, P., et al. 2016, ApJ, 833, 175

Stefansson, G., Li, Y., Mahadevan, S., et al. 2018a, AJ, 156, 266

Stefansson, G., Mahadevan, S., Hebb, L., et al. 2017, ApJ, 848, 9

Stefansson, G., Mahadevan, S., Wisniewski, J., et al. 2018b, Proc. SPIE, 10702, 1070250

Storch, N. I., Lai, D., & Anderson, K. R. 2017, MNRAS, 465, 3927

Thao, P. C., Mann, A. W., Johnson, M. C., et al. 2020, AJ, 159, 32

Tinetti, G., Drossart, P., Eccleston, P., et al. 2016, Proc. SPIE, 9904, 99041X

Van Der Walt, S., Colbert, S. C., & Varoquaux, G. 2011, CSE, 13, 22

Van Eylen, V., Albrecht, S., Huang, X., et al. 2019, AJ, 157, 61

Wang, L., & Dai, F. 2019, ApJL, 873, L1

Wildi, F., Blind, N., Reshetov, V., et al. 2017, Proc. SPIE, 10400, 1040018

Williams, J. P., & Cieza, L. A. 2011, ARA&A, 49, 67

Winn, J. N., Fabrycky, D., Albrecht, S., & Johnson, J. A. 2010a, ApJL, 718, L145

Winn, J. N., & Fabrycky, D. C. 2015, ARA&A, 53, 409

Winn, J. N., Johnson, J. A., Albrecht, S., et al. 2009, ApJL, 703, L99

Winn, J. N., Johnson, J. A., Howard, A. W., et al. 2010b, ApJL, 723, L223

Wolfgang, A., Rogers, L. A., & Ford, E. B. 2016, ApJ, 825, 19

Wright, J. T., & Eastman, J. D. 2014, PASP, 126, 838

Wu, Y., & Lithwick, Y. 2011, ApJ, 735, 109

Yee, S. W., Petigura, E. A., & von Braun, K. 2017, ApJ, 836, 77

Zacharias, N., Urban, S. E., Zacharias, M. I., et al. 2004, AJ, 127, 3043

Zechmeister, M., & Kürster, M. 2009, A&A, 496, 577

Zechmeister, M., Reiners, A., Amado, P. J., et al. 2018, A&A, 609, A12

Zeng, L., Jacobsen, S. B., Sasselov, D. D., et al. 2019, PNAS, 116, 9723

Zhang, K., & Hamilton, D. P. 2008, Icar, 193, 267

Zhou, G., Winn, J. N., Newton, E. R., et al. 2020, ApJL, 892, L21